

Vertical Wind Shear in Neptune's Upper Atmosphere Explained with a Modified Thermal Wind Equation

Joshua Tollefson^{a,*}, Imke de Pater^{a,b}, Philip S. Marcus^c, Stacia Luszcz-Cook^d,
Lawrence A. Sromovsky^e, Patrick M. Fry^e, Leigh N. Fletcher^f, Michael H. Wong^b

^a*Department of Earth and Planetary Science, University of California, Berkeley, CA 94720*

^b*Department of Astronomy, University of California, Berkeley, CA 94720*

^c*Department of Mechanical Engineering, University of California, Berkeley, CA 94720*

^d*Department of Astrophysics; American Museum of Natural History 79th Street at Central
Park West, New York, NY 10024*

^e*Space Science and Engineering Center, University of Wisconsin, Madison, WI 53706, USA*

^f*Department of Physics and Astronomy, University of Leicester, University Road, Leicester,
LE1 7RH, UK*

*Corresponding author

1 **Abstract**

2 We present observations of Neptune taken in H-(1.4-1.8 μm) and K'-(2.0-2.4 μm)
3 bands on the nights of July 3, 2013 and August 20, 2014 from the 10-m W.M.
4 Keck II Telescope using NIRC2 coupled to the Adaptive Optics (AO) system. We
5 track the positions of ~ 100 bright atmospheric features over a 4-5 hour window
6 on each night to derive zonal velocities and wind profiles.

7 Our results deviate from the smooth Voyager zonal wind profile from Sromovsky
8 et al. (1993), often by 100-200 m/s, and often by 3-10 times their estimated uncer-
9 tainties. Besides what appears to be a random dispersion, probably due to a mix
10 of unaccounted for measurement errors, eddy motions, vertical wind shear, and
11 wave-generated features that don't follow the mass flow, there is also a system-
12 atic deviation that is wavelength dependent. The H-band profile is best described
13 with a 73–106 m/s shift towards the east for a retrograde flow (i.e., a lessening of
14 the retrograding velocities) from the Voyager profile at the equator. The K'-band
15 profile is consistent with Voyager on both nights.

16 Comparing H and K' contribution functions and K'/H intensities suggests equato-
17 rial H-band features are, on average, deeper than K'-band features. The H-band
18 equatorial features also have greater eastward (less negative) velocities than K'-
19 band features. Differences in zonal wind speed with depth at constant latitude and
20 time imply vertical wind shear. Assuming the average variations in the zonal wind
21 profiles result from wind shear over 3–5 scale heights, we predict vertical wind
22 shears between -1.0 and -2.2 m/(s·km) at the equator (increasing with height).

1 The standard thermal wind equation and meridional thermal profile for Neptune
2 given by Voyager/IRIS spectra predict wind shear of the wrong sign relative to
3 the observations. We consider two effects that reconcile this inconsistency. First,
4 we calculate the meridional temperature gradients at pressures outside the Voy-
5 ager/IRIS narrow sensitivity window required to match our predicted wind shears.
6 Second, we generalize to a thermal wind equation that considers global methane
7 variations and re-derive the temperature structure needed to match the observed
8 wind shear. If methane is uniformly distributed or weakly-varying, the equa-
9 tor must be 2–15 K cooler than the mid latitudes below 1 bar. If methane is
10 strongly-varying, the equator can be 2–3K warmer than the mid latitudes below 1
11 bar, qualitatively consistent with observed temperature contrasts. These findings
12 may imply a stacked-celled circulation pattern in Neptune’s troposphere and lower
13 stratosphere.

14 **1. Introduction**

15 The zonal wind velocities of the giant planets are obtained by tracking bright
16 cloud features in their atmospheres. Sromovsky et al. (1993) created a zonal wind
17 profile for Neptune by constructing a fit to measurements of position and velocity
18 of discrete cloud features by Limaye and Sromovsky (1991) from Voyager 2 images
19 taken in visible wavelengths. Derived velocities were averaged in latitudinal bins
20 and fit to a fourth-order polynomial to create a smooth zonal wind profile, also
21 referred to as the canonical profile. This profile revealed Neptune’s atmospheric
22 winds are extremely strong, despite Neptune receiving minimal solar insolation.
23 Equatorial wind speeds reach up to 400 m/s, some of the fastest in the solar system.

1 Cloud tracking studies have shown significant deviations from Neptune’s canonical
2 wind profile. Limaye and Sromovsky (1991) saw deviations on the order of 50 m/s,
3 particularly in clouds around the vicinity of a Great Dark Spot (GDS) and at
4 Northern latitudes between 25° - 30° N. Sromovsky et al. (1993) found dispersion
5 in cloud velocities from their constructed canonical profile. Hammel and Lockwood
6 (1997) also saw dispersion of velocities in narrow latitude strips from 1995 HST
7 maps. Sromovsky et al. (2001b,c) tracked features in 1996 data and found general
8 agreement with the canonical profile apart from features close to a dark spot. These
9 findings suggest Neptune’s clouds are not all passive tracers for the background
10 winds, but may also be evidence of wind shear, wave propagation from the presence
11 of vortices, such as the GDS, or other local phenomena.

12 Recent fits to the zonal wind profile using near-infrared imaging data show shifts
13 relative to the canonical profile, in addition to the dispersion of clouds at a given
14 latitude noted by earlier studies. Fitzpatrick et al. (2014) tracked dozens of bright
15 atmospheric features using Keck AO images in the H-band and found that a profile
16 with a ~ 180 m/s eastward shift from the canonical profile at the equator best
17 matched the data. Martin et al. (2012) also observed many cloud features in
18 the H-band ($1.6\mu\text{m}$) that appeared to not move with the canonical profile, with
19 differences reaching as large as 500 m/s. Interestingly, Fitzpatrick et al. (2014)
20 also tracked features in K'-band ($2.2\mu\text{m}$) images and found that the derived profile
21 was consistent with the Voyager profile. They suggested that the eastward shift in
22 the H-band profile from the K'-band and Voyager profiles could be due to temporal
23 changes or a wavelength/depth effect.

24 However, the exact mechanisms that drive the dispersion and profile shifts in the

1 zonal winds of Neptune remain largely unresolved. Martin et al. (2012) observed
2 wave-like behavior in the east-west motions of several cloud features with periods
3 close to the 7.2 hr period of the principal semi-diurnal tides from Triton. They
4 suggested that future observations look at the effect of tidal forcing from Triton
5 on the velocities of Neptune’s cloud features. Recent *Kepler* observations did not
6 find signals in photometric light curves corresponding to the periods of Neptune’s
7 major moons, disproving this idea (Simon et al. (2016)). Fitzpatrick et al. (2014)
8 used radiative transfer models to determine the approximate altitudes of clouds
9 and concluded that the differences between their observed wind profiles in H- and
10 K’-bands were too large in magnitude and in the opposite direction than what
11 could be explained by vertical wind shear. Evidence of large north-south velocities
12 in feature motions may be due to vortices or various wave mechanisms but the
13 exact cause of zonal wind variability is unknown.

14 A major drawback to the studies conducted by Martin et al. (2012) and Fitzpatrick
15 et al. (2014) is that they either: imaged at one wavelength, so that differences in
16 wind speed versus atmospheric depth cannot be seen; or performed cloud tracking
17 at two wavelengths on different nights so that the two can not be directly compared.
18 With these issues in mind, we perform analyses similar to Martin et al. (2012) and
19 Fitzpatrick et al. (2014) to test the vertical wind shear hypothesis for zonal wind
20 dispersion on Neptune. We first present observations of Neptune taken in the
21 H-(1.4-1.8 μm) and K’-(2.0-2.4 μm) bands on each of the nights of July 3, 2013
22 and August 20, 2014 and derive zonal wind profiles for each band by tracking the
23 motions of bright cloud features. We remark on observed differences between the
24 H- and K’-band profiles in the equatorial region, leading us to reconsider vertical

1 wind shear as being important, as we observe differences in speeds for features
2 at the same latitudes and time. We then discuss the applicability of the thermal
3 wind equation to model vertical wind shear in Neptune’s troposphere and lower
4 stratosphere from the equator to mid-latitudes. Finally, we examine the physical
5 consequences of vertical wind shear in terms of Neptune’s global circulation.

6 **2. Data**

7 *2.1. Observations and Data Reduction*

8 We observed Neptune’s atmosphere on July 3, 2013 and August 20, 2014 UT from
9 the Keck II Telescope on Mauna Kea, Hawaii at Near-Infrared (NIR) wavelengths.
10 H- ($1.4\text{-}1.8\ \mu\text{m}$) and K'- ($2.0\text{-}2.4\ \mu\text{m}$) band images were taken on both nights with
11 the narrow camera of the NIRC2 instrument coupled to the Adaptive Optics (AO)
12 system. The detector is a 1024×1024 array with a scale of 0.009942 arcsec/pixel
13 in this view (de Pater et al. (2006)).

14 A total of 75 images were taken in each band on July 3, 2013 from 10:48 - 15:09
15 (UT); 100 images were taken in each band on August 20, 2014 from 08:13 - 13:30
16 (UT). An integration time of 60 seconds was used for all images. This provides
17 the best compromise of high signal to noise while minimizing feature smearing
18 and avoiding over-saturating the detector. Moreover, short integration times allow
19 many images to be taken over the observation period and ensure the identification
20 of the same features in successive images. Images were taken in sets of five and al-
21 ternated between the H- and K'-bands, corresponding to a ~ 15 minute separation
22 between image sets in a single band.

1 Images were reduced using standard infrared reduction techniques of sky subtrac-
2 tion, flat fielding, and median-value masking to remove bad pixels. We estimate
3 $< 1\%$ of the total number of pixels are bad, more than half of which are confined
4 to one quadrant of the detector. Care was taken to image Neptune away from this
5 quadrant. Each image was corrected for the geometric distortion of the array us-
6 ing the ‘dewarp’ routines provided by P. Brian Cameron¹, who estimates residual
7 errors at ≤ 0.1 pixels.

8 We photometrically calibrated images using the Elias standard stars (Elias et al.
9 (1982)) HD162208 on July 3, 2013 and HD1160 on August 20, 2014 and converted
10 them to units of I/F, defined as (Hammel et al. (1989)):

$$\frac{I}{F} = \frac{r^2 F_N}{\Omega F_\odot} \quad (1)$$

11 Here, r is the ratio of Neptune’s to Earth’s heliocentric distance in A.U., πF_\odot is
12 the Sun’s flux density at Earth’s orbit, F_N is Neptune’s observed flux density, and
13 Ω is the solid angle subtended by a pixel on the detector.

14 *2.2. Imaging Results*

15 Figure 1 shows calibrated images of Neptune at the beginning and end of each
16 observing night and in each band. Because there were problems in the optical
17 alignment of the AO system on the night of August 20, 2014, we did not achieve
18 expected (diffraction-limited) resolution. This resulted in limited feature tracking

¹<http://www2.keck.hawaii.edu/inst/nirc2/forReDoc/postobserving/dewarp/nirc2dewarp.pro>

1 capabilities for these images. Our viewing is limited to latitudes south of $+50^\circ$
2 due to the sub-Earth latitude of -27 deg..

3 [Figure 1 about here]

4 Cloud features can be seen in both bands on both nights and their general char-
5 acteristics agree with previous observations (e.g. Sromovsky et al. (2001a); Max
6 et al. (2003); Martin et al. (2012); Fitzpatrick et al. (2014)). The brightest clouds
7 stretch along several constant latitude bands centered at the mid-latitudes. On
8 July 3, 2013, we see the largest bright feature centered at about 40°N . By August
9 20, 2014, this feature had disappeared or migrated to the dark side of the planet.
10 Instead, we see two bright features in the Southern hemisphere centered at roughly
11 40°S . In the H-band, we also see a feature at Neptune's south pole, seen since the
12 Voyager era (e.g. Smith et al. (1989); Limaye and Sromovsky (1991); Luszcz-Cook
13 et al. (2010); Fitzpatrick et al. (2014); de Pater et al. (2014)). No features are seen
14 immediately south of the equator.

15 Figures 2a and c show single images of Neptune that have been produced by
16 combining the set of July 3, 2013 H- and K'-band images, respectively, using a
17 procedure described in Fry et al. (2012). The image combination increases the
18 S/N ratio of the images by employing a pixel brightness averaging method and
19 correcting for feature motions induced by rotation and the canonical zonal wind
20 profile. We did not make such images for August 20, 2014 due to the poor AO
21 performance. Figures 2b and d are Figures 2a and c passed through a high-pass
22 filter by subtracting a median-smoothed image. Banding at the equator can be
23 made out as well as several subtle features. More features can be identified around

1 the equator in the H-band compared to the K'-band.

2 [Figure 2 about here]

3 *2.3. Image Navigation and Projection*

4 Accurate navigation and feature tracking requires precise determinations of Nep-
5 tune's center in each image. An offset of even one pixel in the image centering can
6 dramatically alter an image's projection and the determination of feature loca-
7 tions. This is seen in Figure 4 of Martin et al. (2012), which shows the errors due
8 to a shift in the center of the disk in a map projection. We derive image centers
9 by fitting the observed positions of three moons to their orbits as generated by the
10 Rings Node of NASA's Planetary Data System (<http://pds-rings.seti.org/>) with a
11 χ^2 minimization routine using a method developed by Luszcz-Cook et al. (2010)
12 and used by Fitzpatrick et al. (2014). The error in image center was estimated
13 by the variance in observed orbit to modeled orbit modified by a factor of the
14 reduced χ^2 . The estimated mean uncertainty of the center in both the H- and
15 K'-band images on each night is between 0.1 - 0.2 pixels in x and y coordinates.

16 The accuracy of this procedure can be judged in Figure 3. Shown are the mean
17 images of the aligned image stacks in each band on July 3, 2013. Each averaged
18 image was passed through a high-pass filter by subtracting a median-smoothed
19 image. This allows the individual orbits of Despina, Galatea, and Larissa to be
20 resolved. Overlain on each image are the Rings Node moon orbits, which align
21 well with the observed orbits after image alignment and navigation.

22 [Figure 3 about here]

1 Images are then projected onto a rectangular grid and averaged over the five frames
2 within each image set, with the rotation rate of the planet removed (about 16.11
3 hr, or $1.86^\circ/5$ min). Generally, the zonal drift rates are smaller ($< 0.65^\circ/5$ min)
4 than the angular resolution at disk center ($\sim 2.4^\circ$). Hence, averaging images
5 does not significantly smear features, but increases the signal-to-noise and allows
6 fainter features to be distinguished. Averaging sets of data yielded 15 images in
7 both bands on July 3, 2013 and 20 images in both bands on August 20, 2014.

8 **3. Atmospheric Feature Tracking**

9 The velocities of cloud features act as tracers for atmospheric wind velocities.
10 Figure 4 is a rectangular projection of Figures 2a and c and shows candidate
11 features identified for tracking. Features which are bright and morphologically
12 stable over ~ 1 hour are candidates for tracking. Moreover, a feature must be
13 distinct in longitude and latitude to be considered for tracking. In both bands,
14 trackable features are most common at the mid-latitudes. Near the equator, both
15 bands are relatively dark, with slightly more trackable features in H-band compared
16 to K'-band.

17 [Figure 4 about here]

18 The procedure for extracting wind velocities from feature positions is described
19 in detail in Sromovsky et al. (2012). To summarize, from the projected, averaged
20 images we produce strips of images in a fixed latitude range stacked in a vertical
21 time series. An example of this image stack is given in Figure 5. For each visible
22 feature, a reference image is chosen and centered around a target box containing

1 the feature and a region outside it. Target boxes are placed in all other image
2 strips based on the Voyager canonical longitudinal drift rates for Neptune and
3 their positions are adjusted to maximize the cross-correlation between the feature
4 signals in the reference target box and those in the other images. The centers
5 of each box are the predicted longitude and latitude of the feature in each image.
6 Figure 6 gives an example output of this method, which plots the predicted centers
7 and correlation for each time slice of one feature.

8 [Figure 5 about here]

9 [Figure 6 about here]

10 Measured longitudes and latitudes vs. time were fit to straight lines with weighted
11 regressions. Errors in position are given as the RMS deviation from a straight
12 line. We repeat this procedure for dozens of features. In Figures 7 and 8 we
13 plot the longitude position of selected tracked features versus time. Plots for all
14 features can be found in Supplementary Materials 2. While most features, within
15 their estimated error, follow the drift rates expected by the canonical profile, many
16 deviate significantly. Differences from the anticipated drift rate could be real or
17 due to measurement errors and will be further discussed in later sections. Tables
18 1–4 in Supplementary Materials 1 summarize all tracked feature information.

19 [Figure 7 about here]

20 [Figure 8 about here]

1 4. Results

2 4.1. Zonal Wind Profiles

3 Longitudinal and latitudinal drift rates are transformed into zonal and meridional
4 velocities by the following equations for planetocentric latitudes (Sromovsky et al.
5 (2001b)):

$$V_{\text{lon}} = \frac{R_{\text{eq}}}{\sqrt{1 + \frac{R_{\text{eq}}^2}{R_{\text{pol}}^2} \tan^2 \theta}} \frac{d\phi}{dt} \quad (2)$$

$$V_{\text{lat}} = \frac{R_{\text{pol}}^2}{R_{\text{eq}}} \left(\frac{1 + \frac{R_{\text{eq}}^4}{R_{\text{pol}}^4} \tan^2 \theta}{1 + \frac{R_{\text{eq}}^2}{R_{\text{pol}}^2} \tan^2 \theta} \right)^{\frac{3}{2}} \frac{d\theta}{dt} \quad (3)$$

6 Here, V is the wind speed in m/s, R_{eq} and R_{pol} are the equatorial and polar
7 radii of Neptune, equal to 2.4766×10^7 m and 2.4342×10^7 m respectively (Lindal
8 (1992)). $d\theta/dt$ and $d\phi/dt$ are the derived zonal and meridional drift rates (rad/s).
9 Velocities for each feature are then plotted as a function of latitude and fit to
10 a fourth-order polynomial symmetric about the equator. Neptune rotates from
11 west to east, in the same direction as Earth, and eastward winds are taken to be
12 positive. Thus the equatorial winds on Neptune are retrograde, blowing opposite to
13 the direction of the planet's rotation, unlike Jupiter and Saturn, where equatorial
14 winds are eastward and prograde. Comparisons to our profiles in both bands and
15 the canonical profile are shown in Figures 9 and 10. Table 1 lists the parameters
16 of each fitted polynomial and their widths of uncertainty.

1 [Figure 9 about here]

2 [Figure 10 about here]

3 A significant, large spread in the individual derived zonal velocities is observed
4 at constant latitudes on both nights. This is most prominent at the equator and
5 mid-latitudes in both bands, with differences in feature velocities reaching as high
6 as 500-600 m/s. Moreover, there is a pronounced difference between the derived H
7 and K' zonal wind profiles near the equator. At the equator on July 3, 2013, the
8 deviation in the H-band wind speeds compared to those derived by the Voyager fit
9 is 73 ± 16 m/s. The difference between the H- and K'-bands on this night at the
10 equator is 90 ± 45 m/s. This shift persists in the August 20, 2014 observations.
11 There is a 93 ± 29 m/s deviation between the H-band and canonical profile and
12 a 141 ± 63 m/s difference between the H- and K'-bands on this night. There is
13 no significant difference between the K'-band and Voyager profile on either night.
14 The difference between the H-band and Voyager profiles qualitatively agree with
15 Fitzpatrick et al. (2014), although their H-band velocities are best described by a
16 profile shifted toward positive velocities by 180 ± 50 m/s. The dispersion of our
17 new results falls within the wide range seen in previous publications. Spreads in
18 feature velocity were first seen in measurements of the motions of small clouds in
19 Voyager 2 data, particularly around the GDS and Dark Spot 2 (Smith et al. (1989);
20 Limaye and Sromovsky (1991)). Martin et al. (2012) found large spreads in zonal
21 velocities at constant latitudes in Keck AO H-band observations. Comparatively,
22 at the southern low- and mid-latitudes, the Voyager data show much less dispersion
23 from the canonical profile than the results of Martin et al. (2012). Fitzpatrick et al.
24 (2014) also observed significant deviation in H-band features at the equator and

1 southern-mid latitudes compared to the Voyager profile, with differences reaching
2 as high as ~ 500 m/s.

3 Spurious data affect the fit. Such data could be due to a number of factors in-
4 cluding features near the edge of Neptune's circumference becoming smeared from
5 projection, changes in cloud morphology, limb-brightening, navigation errors, and
6 errors in the position extraction procedure. Several features also move in oscil-
7 latory patterns (as in Martin et al. (2012)) and limited tracking times may not
8 capture a feature's full period of motion. Similar effects were seen on Uranus due
9 to inertial oscillations (Sromovsky and Fry (2005)). Figures 9 and 10 show the
10 individual feature velocities and their 1σ errors alongside the zonal wind profiles.
11 Each feature's plot symbol is proportional to its tracking time. Features tracked
12 over the entire observing period generally have smaller errors than those tracked in
13 only a few images and tend to lie closer to their band's zonal wind profile. Thus,
14 the spread in feature velocities at a fixed latitude is partially a result of their
15 limited tracking time and measurement errors. Figures 11 and 12 show features
16 which have velocity errors less than 30 m/s and were tracked in at least 10 images
17 (~ 2.5 hours). These features are usually bright and morphologically stable and
18 are likely to follow the zonal flow. Spreads in feature velocities up to ~ 200 m/s
19 at constant latitudes are still seen on both nights and both bands, although this is
20 far less than the spread of 500-600 m/s seen with the full set of tracked features.
21 This suggests that large, bright features are less dispersed from the derived zonal
22 profile. It is also true that such features are less susceptible to tracking errors,
23 which might also account for much of their reduced dispersion. This is consis-
24 tent with Martin et al. (2012), who also found that the brightest features usually

1 agreed with the canonical profile. However, we still find that the H- and K'-bands
2 zonal wind profiles still differ by more than 1σ at the equator. The H-band and
3 canonical profiles also differ by 2σ at the equator.

4 [Figure 11 about here]

5 [Figure 12 about here]

6 The meridional wind velocities for each tracked feature are plotted in Figures 13
7 and 14. Globally, the latitudinal velocities are consistent with zero. But, a few
8 features have latitudinal velocities as large as 100–200 m/s. The zonal velocity of
9 these features tend to significantly deviate from the canonical profile, suggesting
10 they are driven by mechanisms that produce motion in both directions, such as
11 vortices or wave mechanisms. This behavior was found by Sromovsky et al. (2001)
12 in HST observations, where several features near the same longitude as a dark spot,
13 but widely scattered in latitude, were accurately measured (within 10–20 m/s) to
14 have meridional wind speeds around 100 m/s, and zonal winds that deviated from
15 the canonical profile by over 200 m/s, while the vast majority of their tracked
16 clouds had insignificant meridional motions and very small deviations from the
17 canonical profile. However, our features with this behavior also have large errors
18 and are not tracked for very long. As previously mentioned, the centers and
19 velocities of features that are faint, ephemeral, or close to the limb, are difficult to
20 constrain.

21 [Figure 13 about here]

22 [Figure 14 about here]

1 4.2. Trends in Feature Depth and Velocity

2 The derived H and K' profiles give a crude 3D look into Neptune's upper at-
3 mosphere since these bands probe different altitudes. We hypothesize that the
4 equatorial shift in the H-band profile is due to deep features. Our data are spec-
5 trally limited so accurate cloud top pressures can not be determined. However, the
6 K'-to-H I/F ratio indicates whether features are deeper or shallower relative to one-
7 another: the deeper a cloud is in the atmosphere, the greater the expected H-band
8 intensity relative to the K'-band intensity. We compute the maximum allowed
9 K'-to-H I/F ratio for each 2013 H-band feature and compare this to their latitude
10 and zonal velocity (see Table 5 in Supplementary Materials 1). Uncertainties are
11 estimated as 20% of I/F, from the uncertainty in the photometry. Figure 15 plots
12 the maximum K'-to-H I/F ratio vs. latitude of each H-band feature. We find equa-
13 torial features ($\pm 20^\circ$) have smaller K'/H intensities than those at mid-latitudes,
14 suggesting they are deeper. This is consistent with Fitzpatrick et al. (2014), who
15 found that clouds at equatorial latitudes are uniformly deeper (~ 0.5 bar) than
16 those at northern mid-latitudes (~ 0.1 bar). Numerous authors also find northern
17 features at the highest altitudes (Sromovsky et al. (2001b); Gibbard et al. (2003);
18 Luszcz-Cook (2012); de Pater et al. (2014)), generally in the stratosphere at the
19 ~ 10 mbar level, although exact pressures vary due to spectral limitations, instru-
20 ment sensitivity at different altitudes, and model assumptions. Luszcz-Cook et al.
21 (2010) compared observed and modeled K'/H and K'/J intensities to determine
22 upper altitudes for south polar features and found that a K'/H ratio of 10% gave
23 a minimum cloud top pressure of 0.4 bar. Features seen in H but not K' may also
24 be deep, with pressures greater than 1 bar. A notable example of this is the south

1 polar feature, observed in H-band but not in K', located at 1.6 bar (de Pater et al.
2 (2014)). We tracked 29 and 20 H-band features in our 2013 and 2014 observations,
3 respectively, that were equatorward of 20° N/S, but only 10 (in 2013) and 11 (in
4 2014) K'-band features in this same region. Taken altogether, we argue that the
5 H-band zonal wind profile represents features which are, on average, deeper than
6 those given in the K'-band profile at low latitudes.

7 [Figure 15 about here]

8 Figure 15 plots the zonal velocity difference from the derived K'-profile vs. lati-
9 tude for each 2013 H-band features. The difference between the H- and K'-band
10 profiles (from Fig. 9) is overplotted. Positive values indicate velocities eastward
11 (less negative) relative to the K'-profile. The largest deviations from the K' profile
12 are around the equator, where features have low K'/H intensities and are probably
13 deep. The deviations in zonal velocity of features at the southern midlatitudes lie
14 closer to zero and are mostly within the uncertainty of the K' profile fit. This is
15 consistent with our hypothesis: the shift in H-band profile may be driven by a
16 handful of deep features around the equator.

17 [Figure 16 about here]

18 Previous studies have also shown that the brightest H-band features are typically
19 at greater depths (pressures) than the brightest K'-band features (Gibbard et al.
20 (2003); Luszcz-Cook (2012); de Pater et al. (2014)). This is consistent with our
21 expectations from radiative transfer modeling. Figure 16 shows the contribution
22 functions for each filter in three different atmospheric models, illustrating the
23 range of depths from which the H- and K'- reflectivity may arise. In all three

1 cases, the gas opacity is dominated by H₂ collision-induced absorption and CH₄
2 absorption. All models include a vertically thin cloud at 3 bar with a 1.6 μm
3 optical depth of 0.5; models b) and c) contain additional aerosols in the upper
4 troposphere/stratosphere, as described in the figure caption. For the purposes
5 of our models in the following sections, we assume that the H-band features are
6 located at 1–2 bar, while K'-band features are located between 10–100 mbar.

7 **5. Interpreting Differences in The H and K' Zonal Wind Profiles**

8 The major caveat to current and past zonal wind profiles is that they are merely
9 best fits to the data. These fits do not pick up any fine scale structure in the
10 zonal winds. Moreover, the profiles represent features driven by a number of
11 possible mechanisms, including shear, wave phenomena, or other local dynamics.
12 Dispersion is partly due to faint, ephemeral features, whose exact centers and
13 velocities may be difficult to pinpoint. Thus, explaining all variations in zonal
14 velocity from these profiles is difficult, if not impossible, to do.

15 We also note that our following models assume that the derived zonal flow is set
16 at a constant pressure level. However, tracked features are not necessarily at the
17 same altitude. For instance, northern mid-latitude features appear at the highest
18 altitudes on Neptune (Sromovsky et al. (2001b); Gibbard et al. (2003); Luszcz-
19 Cook (2012); Fitzpatrick et al. (2014); de Pater et al. (2014)). Irwin et al. (2016)
20 analyzed VLT/SINFONI H-band observations made in 2013 and found bright,
21 deep seated clouds ($P > 1$ bar) in the southern mid-latitudes and ‘intermediate’
22 clouds ($300 < P < 400$ mbar) in the near-equatorial region. Moreover, features
23 at constant latitudes may have different altitudes. De Pater et al. 2014 saw

1 NIR clouds in the southern midlatitudes at two levels: in the stratosphere from
2 0.02-0.03 bar and at altitudes below 0.3 bar ($P > 0.3$ bar). Luszcz-Cook (2012)
3 observed similar altitude variations in Keck OSIRIS data.

4 With these limitations in mind, we only attempt to explain the mean ~ 100 m/s
5 eastward offset in the equatorial region in the H profile from the canonical and
6 K' profiles. This difference seems real (greater than 2σ) and persistent, seen in
7 2009 (Fitzpatrick et al. (2014)) and now in both our 2013 and 2014 observations.
8 Fry and Sromovsky (2004) also show that H-band wind results from 202 cloud
9 measurements taken in 2003 and 2004 images also fall below the canonical profile
10 at low latitudes. Based on the K'/H intensity trends and previous NIR studies,
11 we interpret the H-band profile in the equatorial region as the “average” zonal
12 velocity of features which are mostly: 1) deep (greater than 1 bar), and 2) have
13 velocities shifted $\sim +100$ m/s from the K'-profile. Likewise, we interpret the K'-
14 band profile in the equatorial region as the “average” zonal velocity of features
15 which are mostly: 1) located in stratosphere (around ~ 10 mbar), and 2) have
16 velocities shifted ~ -100 m/s from the H-profile. Differences in the zonal winds
17 with depth at constant latitude and time is evidence of vertical wind shear in
18 Neptune's troposphere and stratosphere. Our derived profiles suggest a wind shear
19 around -100 m/s over several scale heights at the equator (increasing with height).

20 The Voyager results of Sromovsky et al. (1993) also provide evidence of vertical
21 wind shear. Their Figure 15 shows that three major long-lived cloud features,
22 including the GDS, Scooter, and the Second Dark Spot, all move in the same
23 direction as the canonical profile, but with reduced speed. If these major features
24 are more deeply rooted than the small clouds on which the canonical profile is

1 based, and there is spectral evidence that this is true for Scooter, then it would
2 appear that this is another example of the magnitude of wind speeds increasing
3 (becoming more westward) with altitude. Based on Voyager 2/IRIS temperature
4 retrievals alone, this produces the wrong sign of vertical wind shear in the thermal
5 wind equation, as explained below.

6 *5.1. Modeling Vertical Wind Shear at the Equator with the Thermal Wind Equa-*
7 *tion*

8 In this section, we will examine the plausibility of vertical wind shear modeled
9 with the thermal wind equation as an explanation for the observations. The
10 largest and most meaningful differences (i.e. smallest uncertainty) between the
11 H- and K'-band zonal wind profiles occur at the equator. In the following text,
12 we discuss the applicability of the thermal wind equation to Neptune and how it
13 may be extended to the equator under certain conditions, despite the Coriolis force
14 vanishing there. Using plausible depths for the H- and K'-band profiles, discussed
15 in the previous section, we then show that integrating the thermal wind equa-
16 tion does not reproduce the predicted vertical wind shear at the equator. Finally,
17 we discuss the importance of methane variability in modeling the vertical wind
18 shear and how it can reconcile the inconsistency between the observed wind shear
19 and the thermal wind equation. We stress that these results are speculative since
20 they rely on assumptions about the symmetric structure of the zonal wind and
21 temperature fields as well as the exact pressures of H- and K'-band features.

22 The standard thermal wind equation is:

$$23 \quad f_0 \sin \theta \frac{\partial u}{\partial r} = -\frac{g}{r_0 T} \frac{\partial T}{\partial \theta}, \quad (4)$$

1 where $f_0 \equiv 2\Omega_0$ is the Coriolis parameter at the North Pole, rather than the local
 2 Coriolis parameter. We define: r_0 as the radius of the planet, T as the temperature,
 3 $\partial T/\partial\theta$ as the latitudinal-temperature gradient as constant pressure P , g as the
 4 gravity in the $\hat{\mathbf{r}}$ direction, and u is the zonal (longitudinal) velocity.

5 Although the standard thermal wind equation is used in many planetary atmo-
 6 spheric applications and is derived in many texts, c.f., Pedlosky (1987), it is limited
 7 in its use due to the divergence of the Coriolis force near the equator. Marcus et al.
 8 (2017) derive an equatorial thermal wind equation (EQTWE) which provides a
 9 relationship between the vertical wind shear and the horizontal temperature gra-
 10 dients that is valid at and near the equator:

$$11 \quad f_0 \frac{\partial u}{\partial r} = -\frac{g}{r_0 T} \frac{\partial^2 T}{\partial \theta^2} \quad (5)$$

12 A similar result was noted as equation 8.2.2 in Andrews et al. (1987). This equation
 13 is derived by assuming $\partial T/\partial\theta \equiv 0$ and taking L'Hôpital's rule of the standard
 14 thermal wind equation in the limit as $\theta \rightarrow 0$. One problem with using L'Hôpital's
 15 rule in this fashion is that it creates a singularity at the equator if $\partial T/\partial\theta \neq 0$ there.
 16 The EQTWE derived by Marcus et al. (2017) does not require mirror-symmetric
 17 flow and does not produce this singularity.

18 It is seen by inspection that integrating both (4) and (5) upward will not reproduce
 19 the observed H and K'-band equatorial differences. As the zonal winds become
 20 more negative (westward) with altitude (H-band to K'-band), $du/dr < 0$. This
 21 implies that the meridional temperature gradient and its second derivative at the
 22 equator to mid latitudes must be positive. However, this is inconsistent with
 23 derived temperature profiles of Neptune's troposphere from Voyager/IRIS spectra

1 in Figure 17, which show that the equator and poles are warm and the mid-latitude
2 are cool and $\partial^2 T / \partial \theta^2 < 0$ at the equator. (Fletcher et al. (2014)).

3 [Figure 17 about here]

4 In the next two sections, we discuss two reasons that could reconcile the inconsis-
5 tency between the derived zonal wind profiles and temperature profile. First, we
6 discuss whether the assumed temperature profile is correct. Second, we examine
7 the impact non-ideal gas behavior has on the thermal wind equation. In particular,
8 we focus on the latter (our preferred) explanation in the subsequent discussion.

9 5.1.1. *Temperature Profile Incorrect?*

10 Our temperature data come from inbound Voyager/IRIS maps, which are only
11 sensitive to the 70-800 mbar range (Conrath et al. (1991); Fletcher et al. (2014)).
12 Temperatures above and below these pressures are smooth relaxations to an *a pri-*
13 *ori* profile based on the mean stratospheric temperature and the profile from Moses
14 et al. (2005). So, while average global temperatures are known throughout the up-
15 per atmosphere, the meridional trends are more uncertain outside 70-800 mbar.
16 This can be seen in the data itself. In Figure 18 we plot sample inbound tempera-
17 ture data with error bars inside and outside the 70-800 mbar range. At pressures
18 outside this range, the uncertainties become larger, approaching the temperature
19 difference between the equator and mid-latitudes. We can not confidently infer
20 whether the equator is warmer or colder than the mid-latitudes outside 70-800
21 mbar from the current data alone.

22 [Figure 18 about here]

1 We now explore whether meridional variations in temperature outside the well-
 2 constrained 70-800 mbar pressure range could cause wind shear consistent with
 3 the difference between our H and K' observations. We break this calculation into
 4 two steps.

5 First, we calculate the wind shear du/dr between the depth of the K'-band pro-
 6 file down to 1 bar. We do this by using the temperature profile given by the
 7 Voyager/IRIS spectra (Fig. 17) to determine the expected zonal wind profile at 1
 8 bar assuming the K'-profile is at a set pressure level. Since the depth of the K'
 9 features are not precisely constrained, we test a range of pressures from 10 to 100
 10 mbar. The value du/dr is the difference in the zonal winds between the extrap-
 11 lated profile at 1 bar and the H-band, which we also set to a variety of pressures
 12 between 1.0 - 2.4 bar, 2.4 bar being the location of a commonly assumed optically
 13 thick bottom cloud (Irwin et al. (2011)). Altitude changes are calculated assum-
 14 ing hydrostatic equilibrium with a scale height of 19.1 km in the troposphere and
 15 lower stratosphere, a value obtained from de Pater et al. (2014). Voyager/IRIS
 16 derived meridional temperatures are sampled every 5° latitude, which is too sparse
 17 to reliably numerically differentiate. To circumvent this issue, we fit a symmetric
 18 profile to the temperature data:

$$T(\theta) = \sum_{n=0}^N a_n \cos(n\theta) \quad (6)$$

19 One problem with this assumption is evidence of seasonal variations in Neptune's
 20 atmospheric brightness that could cause differences in hemispheric temperatures

1 (Sromovsky et al. (2003); Hammel and Lockwood (2007)). Fletcher et al. (2014)
 2 and de Pater et al. (2014) estimate random uncertainty in the Voyager/IRIS
 3 temperatures to be 1-2 K in the troposphere, increasing to 2-4 K in the mid-
 4 stratosphere. The temperature difference predicted from Voyager/IRIS between
 5 hemispheres at constant latitude is close to or within this error, so our chosen
 6 temperature profile is consistent with meridional symmetry. We now evaluate the
 7 derivative of (6) divided by $\sin \theta$:

$$\frac{1}{\sin \theta} \frac{\partial T}{\partial \theta} = -\frac{1}{\sin \theta} \sum_{n=1}^N n a_n \sin(n\theta) \quad (7)$$

$$= -\sum_{n=1}^N n a_n [\sin(n\theta)/\sin \theta] \quad (8)$$

8 It can be shown that the ratio of sines in the summation is:

$$9 \quad \sin(n\theta)/\sin \theta = \begin{cases} 2[\cos((n-1)\theta) + \cos((n-3)\theta) + \dots + \cos(3\theta) + \cos(\theta)] & : n \text{ even} \\ 2[\cos((n-1)\theta) + \cos((n-3)\theta) + \dots + \cos(4\theta) + \cos(2\theta) + 1/2] & : n \text{ odd} \end{cases}$$

10 We substitute the above expression and equations (6) and (7) into equation (4) to
 11 obtain a numeric thermal wind equation.

12 One problem with this formulation is that the coefficient a_N with the highest or-
 13 der will contribute the most to the derivative at lower latitudes. To mitigate this
 14 effect, we must fit the temperature to as low an order as possible while maintain-
 15 ing a reasonable fit. Table 3 compares various errors of the fit to the observed
 16 temperature data as a function of pressure and fitting degree. We choose to use

1 $N = 4$ which is the lowest order that provides a reasonable fit to the temperature
 2 data.

3 Second, we solve for the meridional temperature structure needed to reproduce
 4 the vertical wind shear between the 1 bar zonal wind profile (calculated in the first
 5 step) and that at the pressure of the H-band profile. This is done by integrating
 6 (4) and (5) and solving for $T(\theta, P)$. We choose 1 bar as the upper limit to the
 7 constructed temperature profiles for two reasons: 1) From de Pater et al. (2014),
 8 the equatorial H-band features not seen in K' must be below 1 bar; 2) If we placed
 9 our limit at the edge of the Voyager/IRIS range, unphysical discontinuities in the
 10 temperature structure would arise. Placing the limit at 1 bar allows reasonable
 11 'smoothing' in the temperature structure between 800 mbar and 1 bar.

12 Away from the equator, we solve for the meridional temperature structure with
 13 the standard thermal wind equation where we integrate this equation with respect
 14 to a reference latitude θ_0 at a particular pressure P :

$$2\Omega \int_{\theta_0}^{\theta} \sin \theta' \frac{du(\theta', P)}{dr} d\theta' = -\frac{g}{r_0} \int \frac{1}{T(\theta, P)} dT, \quad (9)$$

15 and then solve for $T(\theta, P)$:

$$\log \left(\frac{T(\theta, P)}{T_0(P)} \right) = -\frac{2\Omega r_0}{g} \int_{\theta_0}^{\theta} \sin \theta' \frac{du(\theta', P)}{dr} d\theta'. \quad (10)$$

16 Here, $T_0(P)$ is the temperature at θ_0 . The extrapolated zonal wind profile at 1

1 bar from the K'-band profile can be fit to a fourth-order polynomial in degrees
 2 latitude, as was done with the H- and K'-band profiles. So, the total vertical wind
 3 shear can be written as²:

$$\frac{\partial u}{\partial r} = p_0 + p_1 \cdot \theta^2 + p_2 \cdot \theta^4 \quad (11)$$

4 Note that θ is converted from degrees to radians for the purposes of integration.
 5 Furthermore, this procedure assumes du/dr is constant with pressure (although
 6 still a function of latitude) so the resultant temperature structure will represent
 7 an 'average' profile. $p_0, p_1,$ and p_2 do not depend on latitude (though they depend
 8 on the pressure the K'-band is placed). Equation (9) becomes:

$$\log \left(\frac{T(\theta, P)}{T_0(P)} \right) = - \frac{2\Omega r_0}{g} \int_{\theta_0}^{\theta} \sin \theta' \frac{du(\theta', P)}{dr} d\theta' \quad (12)$$

$$= - \frac{2\Omega r_0}{g} \int_{\theta_0}^{\theta} \sin \theta' (p_0 + p_1 \theta'^2 + p_2 \theta'^4) d\theta' \quad (13)$$

9 The integral on the right-hand side of can be solved analytically via repeated
 10 integration-by-parts. The final solution, written for brevity, is:

²We use fourth-order polynomial fits in latitude to the vertical wind shear, instead of Legendre polynomials in $\sin \theta$ for two reasons. First, while the solution to Laplace's equation on a sphere are expressed in terms of Legendre polynomials in $\sin \theta$ (and are used to fit the zonal wind profile for Uranus in Sromovsky et al. (2009)), this is only especially necessary close to the poles, whereas we are doing a local expansion near the equator. Second, we feel it best to use fourth-order fits in latitude since this is the most common fit in the literature to the zonal wind profiles for Neptune. In the Appendix, we show an example demonstrating that using a Legendre expansion does not change the qualitative interpretation of the temperature profile from the equator to mid-latitudes.

$$\log \left(\frac{T(\theta, P)}{T_0(P)} \right) = -\frac{2\Omega r_0}{g} (p_0 \cdot t_0 + p_1 \cdot t_1 + p_2 \cdot t_2) \quad (14)$$

$$T(\theta, P) = T_0(P) \cdot \exp \left[-\frac{2\Omega r_0}{g} (p_0 \cdot t_0 + p_1 \cdot t_1 + p_2 \cdot t_2) \right] \quad (15)$$

where:

$$t_0 = -\cos \theta$$

$$t_1 = 2\theta \sin \theta - (\theta^2 - 2) \cos \theta$$

$$t_2 = 4\theta(\theta^2 - 6) \sin \theta - (\theta^4 - 12\theta^2 + 24) \cos \theta$$

1 At and near the equator, we use the EQTWE to solve for the thermal profile.

2 Assuming the same model for the vertical wind shear (35), the EQTWE becomes

3 a second-order differential equation in θ :

$$4 \quad T'' = c \cdot p(\theta)T, \quad (16)$$

5 where $p(\theta) = p_0 + p_1\theta^2 + p_2\theta^4$ and $c = -f_0 r_0/g$. Letting T to be symmetric about

6 the equator:

$$7 \quad T = \sum_{n=0}^{\infty} a_{2n} \theta^{2n}. \quad (17)$$

8 Then:

$$9 \quad T'' = \sum_{n=1}^{\infty} a_{2n} (2n)(2n-1) \theta^{2n-2} \quad (18)$$

1 Change the limits on (18):

$$2 \quad T'' = \sum_{n=0}^{\infty} a_{2n+2}(2n+2)(2n+1)\theta^{2n}. \quad (19)$$

3 Plug these expansions into (16):

$$\sum_{n=0}^{\infty} a_{2n+2}(2n+2)(2n+1)\theta^{2n} = c \cdot p(\theta) \sum_{n=0}^{\infty} a_{2n}\theta^{2n} \quad (20)$$

$$\sum_{n=0}^{\infty} (a_{2n+2}(2n+2)(2n+1) - a_{2n}c \cdot p(\theta))\theta^{2n} = 0 \quad (21)$$

4 The above implies that the relation within the parentheses equals zero for all
 5 powers of θ . The only complication is that $p(\theta)$ also include powers of θ . The
 6 recurrence relation for the constants are below:

$$a_2 = a_0 \frac{c \cdot p_0}{2} \quad (22)$$

$$a_4 = a_2 \frac{c \cdot p_1}{12} \quad (23)$$

$$a_6 = a_4 \frac{c \cdot p_2}{30} \quad (24)$$

$$a_{2n+2} = a_{2n} \frac{c}{(2n+2)(2n+1)} \quad (25)$$

7 a_0 is the equatorial temperature. As an example, set $a_0 = 80\text{K}$ and plug in relevant
 8 values of the constants for Neptune. Then (4) becomes:

$$9 \quad T = 80 + 28.7\theta^2 - 13.4\theta^4 - 0.1\theta^6 + \dots \quad (26)$$

10 To summarize, we have calculated the thermal structure below 1 bar by solving

1 both the standard and equatorial thermal wind equations. The later is valid at and
 2 near the equator while the former is valid away from it. Assuming an equatorial
 3 temperature of 80K, we find that the difference between the modeled temperatures
 4 resulting from these two models is 0.5K at $\pm 20^\circ$ and 0.2 K at $\pm 15^\circ$. The reason
 5 the temperature solution given in (15) is almost equal to the solution given by (26)
 6 near the equator is that (15) is symmetric about the equator (t_0, t_1 , and t_2 are
 7 all even functions). Thus, in the limit as θ goes to 0, the solutions appear similar
 8 near the equator due to L'Hôpital's rule.

9 [Figure 19 about here]

10 Figure 19 shows a contour plot of a temperature profile in Neptune's troposphere
 11 that matches the observed H- and K'-band wind profiles through the thermal
 12 wind equation. The Voyager/IRIS temperature retrievals are plotted for pressures
 13 less than 800 mbar. The temperature solution required to match the observed
 14 equatorial vertical wind shear is shown for pressures greater than 1 bar. We
 15 choose the reference latitude θ_0 to be the equator and $T_0(P)$ to be the mean
 16 global temperature (given by the smooth relaxation to the *a priori*) at P . In this
 17 example, we assumed the K'-band profile corresponds to 10 mbar and the H-band
 18 profile represents the 1.3 bar layer. This solution predicts 10–15 K temperature
 19 differences between the equator and mid-latitudes below 1 bar. In cases where the
 20 H- and K'-band features are further apart in altitude, we predict amplitudes of
 21 around 5–10 K at $P > 1$ bar. Requiring these large temperature contrasts has an
 22 effect on the IRIS flux and will worsen the quality of the spectral fits. This can be
 23 avoided if the H-band profile is moved further outside the IRIS sensitivity window,
 24 say $P > 2$ bar. In this case, the quality of the spectral fit is unaffected, but this

1 may result in unrealistic depths for H-band features.

2 The predicted temperature profile is largely a function of the expected wind shear.
3 Figure 19 represents an altitude change over 4 scale heights. In cases where the H-
4 and K'-band features are further apart, the temperature contrasts are decreased.
5 If the zonal winds change more rapidly with increasing altitude, larger meridional
6 temperature gradients are needed to match the predicted vertical wind shear. If
7 vertical wind shear is not uniform throughout the atmosphere, then the amplitude
8 of temperature variability will change. For instance, if du/dr changes more rapidly
9 below 1 bar than above it, then there is a larger total integral of $dT/d\theta$ between the
10 H-band and 1 bar. This would decrease the latitudinal gradient needed to produce
11 the expected vertical wind shear and could result in temperature contrasts more
12 compatible with expected IRIS spectral fits.

13 *5.1.2. Revisiting the Thermal Wind Equation*

14 The standard thermal wind equation is derived from the vorticity equation in part
15 by assuming the ideal gas law for a single-component gas: $P = \rho RT$. This involves
16 replacing the horizontal gradient of the density with the horizontal temperature
17 gradient. Therefore in a multi-component atmosphere, the thermal wind equation
18 is not correct because the atmosphere's density gradient is due to spatial varia-
19 tions in temperature and in the composition. The later no longer makes the gas
20 constant 'constant' spatially, but turns it into a function of the densities of the
21 components. Generally, in the Earth's atmosphere, the correction to the thermal
22 wind equation is not large because the molar mass of water (the most significant
23 contributor to density variations in the atmosphere) is small compared to the at-

1 mosphere's mean molar mass. However the mean molar mass of the atmosphere of
 2 Neptune (and the other giant gas planets) is small compared to the molar mass of
 3 gases such as methane that cause spatial density variations. If this effect is large
 4 enough to produce significant variations in the meridional density, the thermal
 5 wind equation (4) will be altered. We define the *virtual temperature* T_v as the
 6 temperature at which a dry atmosphere has the same density and total pressure
 7 as an atmosphere with an additional component (Sun et al. (1991)):

$$T_v = \left(1 + \frac{1 - \epsilon}{\epsilon} \frac{q}{1 + q}\right) T \approx \left(1 + \frac{1 - \epsilon}{\epsilon} q\right) T \quad (27)$$

8 Here, $q = \rho_c/\rho_d$ is the mass mixing ratio between the extra constituent and dry
 9 air and $\epsilon = m_c/m_d$ is the ratio of the molar mass of methane to the molar mass
 10 of dry air. For Neptune with methane as the main trace gas, $m_c/m_d \approx 6.96$ and
 11 the virtual temperature is:

$$T_v = (1 - 0.856q) T \quad (28)$$

12 Contrast this with Earth, where water vapor is the main condensible; $m_c/m_d \approx$
 13 0.622 and the virtual temperature is:

$$T_v = (1 + 0.608q) T \quad (29)$$

1 The atomic mass of methane is larger than that of dry air on Neptune, while the
 2 atomic mass of water vapor is smaller than dry air on Earth. Thus, the virtual
 3 temperature will be smaller than the actual temperature on Neptune, while the
 4 virtual temperature is larger on Earth. An equator enhanced in methane (and with
 5 larger q) compared to mid-latitudes will, therefore, have a cold virtual temperature
 6 relative to the mid-latitudes. If the density gradient induced by methane abun-
 7 dance variations is large enough, it may explain the sign of Neptune's apparent
 8 vertical wind shear.

9 Sun et al. (1991) use the concept of virtual temperature to derive a more general
 10 thermal wind equation. We similarly generalize equation (4) by using virtual
 11 temperature:

$$f \frac{\partial u}{\partial r} = - \frac{g}{r_0 T_v} \frac{\partial T_v}{\partial \theta} \Big|_{P, \phi} \quad (30)$$

12 Defining $C = (1 - \epsilon)/\epsilon$, Sun et al. (1991) shows that:

$$f \frac{\partial u}{\partial z} = - \frac{g}{r_0 T} \frac{\partial T}{\partial \theta} - \frac{g}{r_0} \frac{C}{1 + Cq} \frac{\partial q}{\partial \theta} \quad (31)$$

13 Equation (31) is identical to equation (7) of Sun et al. (1991), which we refer
 14 to as the thermal and compositional wind equation. Their study investigated the
 15 effect of horizontal variations in molar mass on vertical wind shear in Neptune and
 16 Uranus. They found that methane depletion at high latitudes compared to low

1 latitudes produced vertical wind shear with opposite sign to vertical wind shear
2 produced by thermal gradients. If the gradient in molar mass is large enough to
3 overcome the thermal term, the zonal wind speed will become more negative with
4 increasing altitude, consistent with our observations.

5 Similar to the previous section, we ask what temperature gradient is needed below
6 1 bar if molar mass gradients also contribute to the vertical wind shear. Karkoschka
7 and Tomasko (2011) found evidence of methane depletion between 1.2 and 3.3 bar
8 at the mid-latitudes in data acquired by the Hubble STIS spectrograph. They de-
9 rived a methane molar mixing ratio of 0.04 (0.28 mass mixing ratio) at the equator
10 and a $\sim 3\times$ depletion at mid-latitudes. Luszcz-Cook et al. (2013) found brightness
11 variations in spatially-resolved millimeter maps of Neptune, suggestive of merid-
12 ional opacity variations. Their models were consistent with mmassesethane from
13 1–4 bar depleted by $2\times$ at mid-latitudes and by $8\times$ at the poles compared to nom-
14 inal values at the equator (0.044 molar mixing ratio). Luszcz-Cook et al. (2016)
15 also find methane variations consistent with Karkoschka and Tomasko (2011). We
16 assume methane is the major source of molar mass variations and that these vari-
17 ations are confined to altitudes below 1 bar but do not otherwise depend on the
18 pressure. We also assume the variation is hemispherically symmetric in order to
19 extend the general thermal wind equation to the equator. Our model reflects
20 the findings of Karkoschka and Tomasko (2011) and is similar to their Figure 8:
21 methane is enriched at the equator, smoothly decreasing to 45°S and remaining
22 constant out to the poles. The model for the methane mass mixing ratio is ex-

1 pressed below:³

$$2 \quad q(\theta) = \begin{cases} q_0 \cos(4\theta) + q_1 : & |\theta| \leq 45 \\ q_1 - q_0 : & |\theta| > 45 \end{cases}$$

3 [Figure 20 about here]

4 Figure 20 plots our methane model assuming $\times 2$ and $\times 4$ depletion at the mid-
 5 latitudes to poles assuming an equator with a molar mixing ratio of 0.04. Figure 21
 6 plots the virtual temperature assuming this model for the methane mixing ratio.
 7 The molecular mass variation due to methane will change the thermal contribution
 8 to the observed vertical wind shear. The new equation to solve is:

9 [Figure 21 about here]

$$2\Omega \sin \theta \frac{\partial u}{\partial r} = -\frac{g}{r_0 T} \frac{\partial T}{\partial \theta} \Big|_P - \frac{g}{r_0} \frac{C}{1 + Cq} \frac{\partial q}{\partial \theta} \Big|_P, \quad (32)$$

10 where we integrate this equation to solve for $T(\theta, P)$:

$$-\frac{g}{r_0} \int \frac{1}{T(\theta, P)} dT = 2\Omega \int_{\theta_0}^{\theta} \sin \theta' \left[\frac{du(\theta', P)}{dr} + \frac{g}{r_0} \frac{C}{1 + Cq} \frac{\partial q}{\partial \theta'} \right] d\theta', \quad (33)$$

$$\log \left(\frac{T(\theta, P)}{T_0(P)} \right) = -\frac{2\Omega r_0}{g} \int_{\theta_0}^{\theta} \sin \theta' \left[\frac{du(\theta', P)}{dr} + \frac{g}{r_0} \frac{C}{1 + Cq} \frac{\partial q}{\partial \theta'} \right] d\theta' \quad (34)$$

³Among many functions we could choose to represent the methane gradient, we picked $\cos(4\theta)$ since its derivative is zero at 45° . This produces a smooth transition in the methane abundance from low-latitudes and high-latitudes, where methane abundance is constant as in Karkoschka and Tomasko (2011).

1 Like before, we assume the vertical wind shear and molar mass term can be fit to
2 fourth-degree polynomials:

$$\frac{\partial u}{\partial r} + \frac{g}{r_0} \frac{C}{1 + Cq} \frac{\partial q}{\partial \theta} = p_0 + p_1 \cdot \theta^2 + p_2 \cdot \theta^4 \quad (35)$$

3 Integrate as before to solve for the temperature profile below 1 bar. The derived
4 temperature profile taking methane variations into account is shown in Figure 22.
5 Our examples illustrate how important the meridional methane distribution is on
6 the derived temperature solutions. In the first case, where methane is depleted by
7 2× at mid-latitudes and poles compared to the equator, we obtain an equator 2–3K
8 colder than the mid-latitudes. In the second case, where methane is depleted by
9 4× at the mid-latitudes compared to the equator and poles, we obtain an equator
10 2–3K warmer than the mid-latitudes. This is qualitatively consistent with the
11 warmer equatorial temperatures observed at $P < 1$ bar by Voyager/IRIS (e.g.
12 Conrath et al. (1998)) and ground-based observations (Fletcher et al. (2014)).

13 [Figure 22 about here]

14 An important caveat to this analysis is that it assumes methane does not condense.
15 Ices are 1000-fold denser than gases and the ideal gas law is no longer applicable.
16 Our model occurs in the heart of methane’s condensation region so these results
17 should be viewed with caution. Nonetheless, the above work demonstrates the ne-
18 cessity of including compositional gradients in models of Neptune’s winds. Future
19 models will need to consider all phases of methane and other heavy species deeper
20 down to accurately calculate Neptune’s density profile.

1 In summary, the meridional temperature structure needed to replicate Neptune's
2 equatorial zonal wind shear depends heavily on the gaseous methane distribution
3 below 1 bar. If methane abundance is globally uniform or weakly varying, then
4 a cold equator relative to the mid-latitudes is needed to explain the vertical wind
5 shear. If methane abundance changes greatly, then a warm equator is permitted.

6 Thermal infrared spectra from Cassini/CIRS observations have been used to derive
7 temperature fields for the stratosphere and troposphere of Jupiter and Saturn and
8 allow us to compare our derived temperatures for Neptune's troposphere. Below
9 $\sim 100\text{--}700$ mbar, both planets have a cool equator with peak meridional contrasts
10 $\sim 2\text{--}10$ K (see Fig. 2 of Simon-Miller et al. (2006) and Fig. 2 of Fletcher et al.
11 (2010)). Zonal wind speeds of Jupiter's deep troposphere were extracted from the
12 Doppler Wind Experiment at 6°N and show an increase in the velocity with depth
13 below 1 bar (Atkinson et al. (1998)). This is consistent with a positive latitudinal
14 temperature gradient (i.e. cool equator) since the wind shear is negative. Numer-
15 ical simulations of off-equatorial jets in Jupiter's and Saturn's upper atmosphere
16 reproduce similar results (Fig. 1 of Liu and Schneider (2015)). However, wind
17 shear near 5-micron hotspots is likely to be complex, because dynamics are af-
18 fected by a planetary-scale wave in addition to zonal-mean gradients (Showman
19 and Dowling (2000)). Neptune's measured tropospheric temperatures are the op-
20 posite to that described on Jupiter and Saturn (i.e., a warm equator instead), but
21 this work could hint at a cool 'Jupiter-like' equator at depths > 1 bar provided
22 a flatter methane distribution. More precise constraints on Neptune's methane
23 profile and extent of zonal flow are needed to determine if Neptune's temperature
24 field is similar to the other jovian planets. Considering the energetics of flow in fu-

1 ture models will also be important for relating Neptune’s zonal winds, temperature
2 field, and composition.

3 *5.2. Global Circulation*

4 Multi-wavelength observations have been crucial for determining Neptune’s global
5 circulation pattern. De Pater et al. 2014 analyzed near-infrared cloud activity,
6 temperature patterns, ortho/para H₂ ratios, and measurements of mid-infrared
7 and radio temperature brightness to construct a hemispherically symmetric circu-
8 lation pattern where air rises above the mid-latitudes and sinks at the equator and
9 poles. Their single-layer circulation is broadly extended, ranging from the strato-
10 sphere down to ~ 40 bar, and could explain most, though not all, observations at
11 wavelengths spanning a range from the visible to 6 cm. If methane abundances are
12 uniform or weakly varying, our data are indicative of a more complicated circula-
13 tion between the equator and mid-latitudes. Below 1 bar, an equator colder than
14 the mid-latitudes is needed to produce the predicted vertical wind shear. This
15 scenario is consistent with air rising and cooling as it adiabatically expands at the
16 equator while air subsides and warms due to adiabatic compression at the mid-
17 latitudes. Such a circulation pattern is consistent with data that do not agree with
18 the single-cell circulation in de Pater et al. (2014). Butler et al. (2012) constructed
19 1-cm radio maps of Neptune from data obtained with the Expanded Very Large
20 Array (EVLA) and found weak brightness enhancements at the southern mid-
21 latitudes, as well as strong enhancements over the pole and equator. Karkoschka
22 and Tomasko (2011) found evidence of methane depletion between 1.2 and 3.3 bar
23 at mid-latitudes in data acquired by the Hubble STIS spectrograph. Regions of
24 low methane abundance and opacity indicate downwelling. Conversely, high abun-

1 dances and opacities suggest upwelling. Moreover, methane-rich air will cool and
2 condense as it rises at the equator. This may explain the presence of deep-seated
3 H-band features. An example two-celled model that is consistent with these ob-
4 servations is given in Figure 23. This modifies the model given by de Pater et al.
5 (2014) below 1 bar to an unknown depth. A three-cell circulation pattern has
6 been proposed for Uranus to explain polar methane depletion and cloud activity
7 at the mid-latitudes (Sromovsky et al. (2014)). Stacked circulation cells above and
8 below the clouds of Saturn may explain spatial distributions of chemical tracers
9 measured by Cassini/VIMS (Fletcher et al. (2011)). Neptune’s atmosphere may
10 be similarly complex.

11 [Figure 23 about here]

12 On the other hand, if methane abundances vary significantly, a warm equator
13 can still reproduce our observed vertical wind shear. Such a temperature profile
14 would be consistent with both: 1) the single-cell circulation model suggested by
15 de Pater et al. (2014), and 2) direct measurements of the temperature field. Al-
16 though the de Pater et al. (2014) model explained a broad range of observations,
17 observed variations in methane abundance are not explained by this circulation
18 model. It is likely that an elaborate circulation model is needed to explain all
19 known observations of Neptune’s upper atmosphere. Neptune’s circulation pat-
20 tern may contain finer latitudinal and vertical structure than we can determine
21 from currently available data.

1 **6. Conclusions**

2 We tracked the longitude-latitude positions of dozens of bright features in Nep-
3 tune’s atmosphere from Keck AO images on July 3, 2013 and August 20, 2014 in
4 the H- and K’-bands. From their positions and length of time tracked, we derived
5 zonal and meridional velocities and constructed zonal wind profiles for each band
6 and night.

7 Our main conclusions are:

8 1. The motions of many individually tracked cloud features are significantly differ-
9 ent than the zonal wind speeds predicted by the canonical profile from Sromovsky
10 et al. (1993). This dispersion is most prominent from the equator to mid-latitudes,
11 reaching as high as 500-600 m/s, and is seen on both nights. A few features have
12 meridional velocities as large as 100-200 m/s. These features also tend to have the
13 largest zonal velocity deviations from the canonical profile, suggesting they are
14 driven by mechanisms like vortices or wave phenomena as these produce motion
15 in both directions. Generally, features with the largest velocity variations (in both
16 directions) have large RMS errors and are tracked for a short time. These features
17 are usually ephemeral, faint, or near the planetary limb, meaning their centers
18 are hard to constrain. Velocity variations also persist in low-error, long-tracked
19 features, although the magnitude of variability is muted.

20 2. There are significant differences in the zonal wind profiles between the H-band
21 and K’-band on both nights. This is most prominent at the equator, where the H
22 profile is best described by a profile shifted eastward by 90 ± 45 m/s on July 3, 2013

1 and 141 ± 63 m/s on August 20, 2014. There is little difference between the K'-band
2 zonal wind profiles and the canonical profile. 2013 H band features have smaller
3 Kp/H I/F ratios at the equator than the mid-latitudes. The exquisite quality of
4 our July 3, 2013 images reveal numerous equatorial features in the H-band that
5 are not present in K'-band. This suggests those features are located below 1 bar.
6 Taken all together, this is consistent with the idea that the mean eastward velocity
7 shifts in the H profile are driven by deep-seated features. Differences in velocity
8 with depth are evidence of vertical wind shear.

9 3. If the shift in the H profile is real and indicative of vertical wind shear, we
10 predict shears between -1.0 to -2.2 m/(s·km) at the equator, assuming H and K'
11 features typically differ in altitude by 3–5 scale heights. Previous studies have
12 dismissed vertical wind shear as an explanation for the variability between the
13 H-band and canonical profile, claiming that thermal winds would decay (be less
14 negative) with increasing altitude and produce the opposite of what is observed.
15 However, this analysis relied on Voyager/IRIS temperature retrievals that are only
16 sensitive between 70–800 mbar, outside the pressures we expect the H-band to see
17 at the equator. Using a formulation that extends the thermal wind equation to
18 the equator (Marcus et al. (2017)), we derived the meridional temperature profiles
19 that are needed below 1 bar to match our predicted vertical wind shear. Neglect-
20 ing density effects due to variation in methane concentration, we find that the
21 equator must be colder than the midlatitudes by 5–15 K to explain the observa-
22 tions, although this range can be lowered if wind shear is not uniform throughout
23 the atmosphere. This is similar to tropospheric temperature profiles derived from
24 mid-infrared observations and numerical simulations of Jupiter' and Saturn's at-

1 mosphere. Colder temperatures at the equator are consistent with upwelling and
2 are not consistent with the de Pater et al. (2014) single-layer model’s equatorial
3 downwelling.

4 4. We used the generalized thermal-compositional wind equation (Sun et al.
5 (1991)) to account for density variations that result from latitudinally fluctuat-
6 ing methane abundances. We used this equation to re-derive the temperature
7 structure below 1 bar needed to match expected methane variations and vertical
8 wind shear. If methane is weakly-depleted at the mid-latitudes ($2\times$ depletion),
9 an equator 2–3 K colder than the mid-latitudes is consistent with our inferred
10 wind shear. This could be explained by adiabatic cooling and methane enrich-
11 ment at the equator due to upwelling, but it is inconsistent with the de Pater
12 et al. (2014) single-layer circulation with equatorial downwelling. If methane is
13 strongly-depleted at mid-latitudes ($4\times$ depletion), an equator 2–3K warmer than
14 the mid-latitudes is consistent with our inferred wind shear. Equatorial warming
15 combined with methane enrichment is not consistent with either the single-layer
16 de Pater et al. (2014) model, or the double-layer model in Fig. 23. It is, how-
17 ever, consistent with observed measurements of Neptune’s temperature field. We
18 emphasize the importance of including these density variations future models, as
19 condensation regions or phase changes result in large density changes.

20 5. Our results suggest a global circulation pattern more complicated than the
21 single-celled, vertically broad model described by de Pater et al. (2014). Stacked
22 circulation cells may explain observed methane variations and our derived temper-
23 ature profiles. However, we can not reconcile all observations of Neptune’s upper
24 atmosphere with this model. Latitudinally and vertically complex circulation cells

1 may be needed to explain the dynamics of Neptune’s atmosphere.

2 Multi-wavelength observations of Neptune are required to fully understand the
3 degree of vertical wind shear and true circulation pattern in the troposphere. Cloud
4 tracking with spectral information would verify whether features with different
5 speeds are in fact at different depths. Radio wavelengths are sensitive to H₂S
6 variations in Neptune’s atmosphere below 1 bar. Longitudinally-resolved radio
7 maps of Jupiter have recently been produced with the upgraded VLA (de Pater
8 et al. (2016)). Similar maps of Neptune’s deep atmosphere would trace variations
9 in the H₂S abundance and determine regions of sinking (low H₂S) and rising (high
10 H₂S) air. This would provide a check for the stacked-celled circulation hypothesis.

11 **7. Acknowledgements**

12 The data presented were obtained at the W.M. Keck Observatory, which is op-
13 erated as a scientific partnership among the California Institute of Technology,
14 the University of California and the National Aeronautics and Space Administra-
15 tion. The Observatory was made possible by the generous financial support of the
16 W.M. Keck Foundation. This work has been supported in part by the National
17 Science Foundation, NSF Grant AST-0908575 and AST-1615004 to UC Berkeley
18 and by NASA Headquarters: under the NASA Earth and Space Science Fellowship
19 program Grant NNX16AP12H to UC Berkeley, and Grant NNX23AG56G under
20 NASA Planetary Atmospheres to UC Berkeley. The authors wish to recognize and
21 acknowledge the very significant cultural role and reverence that the summit of
22 Mauna Kea has always had within the indigenous Hawaiian community. We are
23 most fortunate to conduct observations from this mountain.

1 8. References

2 Andrews, D. G., Holton, J. R., Leovy, C. B., 1987. Middle atmosphere dynamics.
3 Academic press.

4 Atkinson, D. H., Pollack, J. B., Seiff, A., 1998. The Galileo probe doppler wind
5 experiment: Measurement of the deep zonal winds on Jupiter. *Journal of Geo-*
6 *physical Research: Planets* 103 (E10), 22911–22928.
7 URL <http://dx.doi.org/10.1029/98JE00060>

8 Butler, B. J., Hofstadter, M., Gurwell, M., Orton, G., Norwood, J., Oct. 2012. The
9 Deep Atmosphere of Neptune From EVLA Observations. In: AAS/Division for
10 Planetary Sciences Meeting Abstracts. Vol. 44 of AAS/Division for Planetary
11 Sciences Meeting Abstracts. p. 504.06.

12 Conrath, B., Gierasch, P., Ustinov, E. A., 1998. Thermal Structure and Para
13 Hydrogen Fraction on the Outer Planets from Voyager IRIS Measurements.
14 *Icarus* 135, 501–517.

15 Conrath, B. J., Flasar, F. M., Gierasch, P. J., 1991. Thermal structure and dynam-
16 ics of Neptune’s atmosphere from Voyager measurements. *Journal of Geophysical*
17 *Research: Space Physics* 96 (S01), 18931–18939.
18 URL <http://dx.doi.org/10.1029/91JA01859>

19 de Pater, I., Fletcher, L. N., Luszcz-Cook, S., DeBoer, D., Butler, B., Hammel,
20 H. B., Sitko, M. L., Orton, G., Marcus, P. S., 2014. Neptune’s global circulation
21 deduced from multi-wavelength observations. *Icarus* 237, 211–238.
22 URL <http://www.sciencedirect.com/science/article/pii/S001910351400116X>

- 1 de Pater, I., Gibbard, S. G., Hammel, H., 2006. Evolution of the dusty rings of
2 uranus. *Icarus* 180 (1), 186 – 200.
3 URL <http://www.sciencedirect.com/science/article/pii/S0019103505002897>
- 4 de Pater, I., Sault, R. J., Butler, B., DeBoer, D., Wong, M. H., 2016. Peering
5 through Jupiter’s Clouds with the Very Large Array. *Science* (submitted).
- 6 Elias, J. H., Frogel, J. A., Matthews, K., Neugebauer, G., Jul. 1982. Infrared
7 standard stars. *Astronomical Journal* 87, 1029–1034.
- 8 Fitzpatrick, P. J., de Pater, I., Luszcz-Cook, S., Wong, M. H., Hammel, H. B.,
9 2014. Dispersion in Neptune’s zonal wind velocities from NIR Keck AO obser-
10 vations in July 2009. *Astrophysics and Space Science* 350 (1), 65–88.
11 URL <http://dx.doi.org/10.1007/s10509-013-1737-2>
- 12 Fletcher, L. N., Achterberg, R. K., Greathouse, T. K., Orton, G. S., Conrath,
13 B. J., Simon-Miller, A. A., Teanby, N., Guerlet, S., Irwin, P. G., Flasar, F.,
14 2010. Seasonal change on Saturn from Cassini/CIRS observations, 2004-2009.
15 *Icarus* 208 (1), 337 – 352.
16 URL <http://www.sciencedirect.com/science/article/pii/S0019103510000412>
- 17 Fletcher, L. N., Barnes, K., Momary, T. W., Showman, A., Irwin, P., Orton, G. S.,
18 Roos-Serote, M., Merlet, C., 2011. Saturn’s tropospheric composition and clouds
19 from Cassini/VIMS 4.6–5.1 μm nightside spectroscopy. *Icarus* 214, 510–533.
- 20 Fletcher, L. N., de Pater, I., Orton, G. S., Hammel, H. B., Sitko, M. L., Irwin,
21 P. G., 2014. Neptune at summer solstice: Zonal mean temperatures from
22 ground-based observations, 2003–2007. *Icarus* 231, 146–167.
23 URL <http://www.sciencedirect.com/science/article/pii/S0019103513005095>

- 1 Fry, P., Sromovsky, L., 2004. Keck 2 AO Observations of Neptune in 2003 and
2 2004. *Bull. Am. Astron. Soc*, 1103.
- 3 Fry, P. M., Sromovsky, L. M., de Pater, I., Hammel, H. B., Rages, K. A., 2012.
4 Detection and tracking of subtle cloud features on Uranus. *The Astronomical*
5 *Journal* 143 (6), 150–161.
6 URL <http://dx.doi.org/10.1016/j.icarus.2012.05.029>
- 7 Gibbard, S. G., de Pater, I., Roe, H. G., Martin, S., Macintosh, B. A., Max,
8 C. E., 2003. The altitude of Neptune cloud features from high-spatial-resolution
9 near-infrared spectra. *Icarus* 166 (2), 359–374.
10 URL <http://www.sciencedirect.com/science/article/pii/S0019103503002331>
- 11 Hammel, H. B., Baines, K. H., Bergstralh, J. T., 1989. Vertical aerosol structure
12 of Neptune: Constraints from center-to-limb profiles. *Icarus* 80 (2), 416–438.
13 URL <http://www.sciencedirect.com/science/article/pii/0019103589901498>
- 14 Hammel, H. B., Lockwood, G. W., 1997. Atmospheric Structure of Neptune in
15 1994, 1995, and 1996: HST Imaging at Multiple Wavelengths. *Icarus* 129, 466–
16 481.
- 17 Hammel, H. B., Lockwood, G. W., 2007. Suggestive correlations between the
18 brightness of Neptune, solar variability, and Earth’s temperature. *Geophysi-*
19 *cal Research Letters* 34 (8), 108203.
20 URL <http://dx.doi.org/10.1029/2006GL028764>
- 21 Irwin, P., Fletcher, L., Tice, D., Owen, S., Orton, G., Teanby, N., Davis, G., 2016.
22 Time variability of Neptune’s horizontal and vertical cloud structure revealed
23 by VLT/SINFONI and Gemini/NIFS from 2009 to 2013. *Icarus* 271, 418–437.

- 1 Irwin, P. G. J., Teanby, N. A., Davis, G. R., Fletcher, L. N., Orton, G. S., Tice,
2 D., Hurley, J., Calcutt, S. B., 11 2011. Multispectral imaging observations of
3 Neptune's cloud structure with Gemini-North. *Icarus* 216 (1), 141–158.
4 URL <http://www.sciencedirect.com/science/article/pii/S0019103511003149>
- 5 Karkoschka, E., Tomasko, M. G., 2011. The haze and methane distributions on
6 neptune from hststis spectroscopy. *Icarus* 211 (1), 780 – 797.
7 URL <http://www.sciencedirect.com/science/article/pii/S0019103510003192>
- 8 Limaye, S. S., Sromovsky, L. A., 1991. Winds of Neptune: Voyager observations
9 of cloud motions. *Journal of Geophysical Research: Space Physics* 96 (S01),
10 18941–18960.
11 URL <http://dx.doi.org/10.1029/91JA01701>
- 12 Lindal, G. F., Mar. 1992. The atmosphere of Neptune - an analysis of radio occul-
13 tation data acquired with Voyager 2. *Astronomical Journal* 103, 967–982.
- 14 Liu, J., Schneider, T., 2015. Scaling of Off-Equatorial Jets in Giant Planet Atmo-
15 spheres. *Journal of the Atmospheric Sciences* 72 (1), 389 – 408.
- 16 Luszcz-Cook, S., 2012. Millimeter and near-infrared observations of Neptunes at-
17 mospheric dynamics. Ph.D. thesis.
- 18 Luszcz-Cook, S., de Kleer, K., de Pater, I., Adamkovics, M., Hammel, H., 2016.
19 Retrieving Neptune's aerosol properties from Keck {OSIRIS} observations. I.
20 Dark regions. *Icarus* 276, 52–87.
- 21 Luszcz-Cook, S., de Pater, I., Ádámkovics, M., Hammel, H., 2010. Seeing double

- 1 at Neptune's south pole. *Icarus* 208 (2), 938–944.
2 URL <http://www.sciencedirect.com/science/article/pii/S0019103510001090>
- 3 Luszcz-Cook, S., de Pater, I., Wright, M., 2013. Spatially-resolved millimeter-
4 wavelength maps of neptune. *Icarus* 226 (1), 437 – 454.
5 URL <http://www.sciencedirect.com/science/article/pii/S0019103513002194>
- 6 Marcus, P. S., Tollefson, J., de Pater, I., Wong, M. H., 2017. An Equatorial Ther-
7 mal Wind Equation: Applications to Jupiter. *Icarus*.
- 8 Martin, S. C., de Pater, I., Marcus, P., 2012. Neptunes zonal winds from near-IR
9 Keck adaptive optics imaging in August 2001. *Astrophysics and Space Science*
10 337 (1), 65–78.
11 URL <http://dx.doi.org/10.1007/s10509-011-0847-y>
- 12 Max, C. E., Macintosh, B. A., Gibbard, S. G., Gavel, D. T., Roe, H. G., de Pater,
13 I., Ghez, A. M., Acton, D. S., Lai, O., Stomski, P., Wizinowich, P. L., 2003.
14 Cloud structures on Neptune observed with Keck telescope adaptive optics. *The*
15 *Astronomical Journal* 125 (1), 364.
16 URL <http://stacks.iop.org/1538-3881/125/i=1/a=364>
- 17 Moses, J. I., Fouchet, T., Bzard, B., Gladstone, G. R., Lellouch, E., Feuchtgruber,
18 H., 2005. Photochemistry and diffusion in Jupiter's stratosphere: Constraints
19 from ISO observations and comparisons with other giant planets. *Journal of*
20 *Geophysical Research: Planets* 110 (E8), n/a–n/a, e08001.
21 URL <http://dx.doi.org/10.1029/2005JE002411>
- 22 Pedlosky, J., 1987. *Geophysical Fluid Dynsmics*. Springer-Verlag New York.

- 1 Showman, A., Dowling, T., 2000. Nonlinear Simulations of Jupiter's 5-Micron Hot
2 Spots. *Science* 289, 1737–1740.
- 3 Simon, A. A., Rowe, J. F., Gaulme, P., Hammel, H. B., Casewell, S. L., Fortney,
4 J. J., Gizis, J. E., Lissauer, J. J., Morales-Juberias, R., Orton, G. S., Wong,
5 M. H., Marley, M. S., 2016. Neptune's Dynamic Atmosphere from Kepler K2
6 Observations: Implications for Brown Dwarf Light Curve Analyses. *The Astro-
7 physical Journal* 817 (2), 162–171.
- 8 Simon-Miller, A. A., Conrath, B. J., Gierasch, P. J., Orton, G. S., Achterberg,
9 R. K., Flasar, F. M., Fisher, B. M., 2006. Jupiter's atmospheric temperatures:
10 From Voyager IRIS to Cassini CIRS. *Icarus* 180 (1), 98–112.
11 URL <http://www.sciencedirect.com/science/article/pii/S0019103505002733>
- 12 Smith, B. A., Soderblom, L. A., Banfield, D., Barnet, c., Basilevsky, A. T., Beebe,
13 R. F., Bollinger, K., Boyce, J. M., Brahic, A., Briggs, G. A., Brown, R. H.,
14 Chyba, c., Collins, s. A., Colvin, T., Cook, A. F., Crisp, D., Croft, S. K.,
15 Cruikshank, D., Cuzzi, J. N., Danielson, G. E., Davies, M. E., De Jong, E.,
16 Dones, L., Godfrey, D., Goguen, J., Grenier, I., Haemmerle, V. R., Hammel,
17 H., Hansen, c. J., Helfenstein, c. P., Howell, C., Hunt, G. E., Ingersoll, A. P.,
18 Johnson, T. V., Kargel, J., Kirk, R., Kuehn, D. I., Limaye, S., Masursky, H.,
19 McEwen, A., Morrison, D., Owen, T., Owen, W., Pollack, J. B., Porco, c. c.,
20 Rages, K., Rogers, P., Rudy, D., Sagan, C., Schwartz, J., Shoemaker, E. M.,
21 Showalter, M., Sicardy, B., Simonelli, D., Spencer, J., Sromovsky, L. A., Stoker,
22 C., Strom, R. G., Suomi, V. E., Synott, S. P., Terrile, R. J., Thomas, P.,
23 Thompson, W. R., Verbiscer, A., Veverka, J., 1989. Voyager 2 at Neptune:

1 Imaging science results. *Science* 246 (4936), 1422–1449.
2 URL <http://www.sciencemag.org/content/246/4936/1422.abstract>

3 Sromovsky, L., Fry, P., Hammel, H., Ahue, W., de Pater, I., Rages, K., Showalter,
4 M., van Dam, M., 2009. Uranus at equinox: Cloud morphology and dynamics.
5 *Icarus* 203 (1), 265–286.
6 URL <http://www.sciencedirect.com/science/article/pii/S0019103509001729>

7 Sromovsky, L. A., Fry, P. M., 2005. Dynamics of cloud features on Uranus. *Icarus*
8 179 (2), 459–484.

9 Sromovsky, L. A., Fry, P. M., Baines, K. H., Limaye, S. S., Orton, G. S., Dowling,
10 T. E., 2001a. Coordinated 1996 HST and IRTF imaging of Neptune and Triton:
11 I. Observations, navigation, and differential deconvolution. *Icarus* 149 (2),
12 416–434.
13 URL <http://www.sciencedirect.com/science/article/pii/S001910350096562X>

14 Sromovsky, L. A., Fry, P. M., Dowling, T. E., Baines, K. H., Limaye, S. S.,
15 2001b. Coordinated 1996 HST and IRTF Imaging of Neptune and Triton:
16 III. Neptune’s Atmospheric Circulation and Cloud Structure. *Icarus* 149 (2),
17 459–488.
18 URL <http://www.sciencedirect.com/science/article/pii/S0019103500965643>

19 Sromovsky, L. A., Fry, P. M., Dowling, T. E., Baines, K. H., Limaye, S. S., 2001c.
20 Neptune’s Atmospheric Circulation and Cloud Morphology: Changes Revealed
21 by 1998 HST Imaging. *Icarus* 150, 244–260.

22 Sromovsky, L. A., Fry, P. M., Hammel, H. B., de Pater, I., Rages, K. A., 2012.
23 Post-equinox dynamics and polar cloud structure on Uranus. *Icarus* 220 (2),

1 694–712.
2 URL <http://www.sciencedirect.com/science/article/pii/S0019103512002114>

3 Sromovsky, L. A., Fry, P. M., Limaye, S. S., Baines, K. H., 2003. The nature
4 of Neptune’s increasing brightness: evidence for a seasonal response. *Icarus*
5 163 (1), 256–261.
6 URL <http://www.sciencedirect.com/science/article/pii/S0019103503000691>

7 Sromovsky, L. A., Karkoschka, E., Fry, P. M., Hammel, H. B., de Pater, I., Rages,
8 K., 2014. Methane depletion in both polar regions of Uranus inferred from
9 HST/STIS and Keck/NIRC2 observations. *Icarus* 238, 137 – 155.
10 URL <http://www.sciencedirect.com/science/article/pii/S0019103514002693>

11 Sromovsky, L. A., Limaye, S. S., Fry, P. M., 1993. Dynamics of Neptune’s major
12 cloud features. *Icarus* 105 (1), 110–141.
13 URL <http://www.sciencedirect.com/science/article/pii/S0019103583711140>

14 Sun, Z.-P., Stoker, C. R., Schubert, G., 1991. Thermal and humidity winds in
15 outer planet atmospheres. *Icarus* 91 (1), 154–160.

1 9. Appendix

2 In this appendix, we show an alternate model for the vertical wind shear: $\partial u/\partial r$
 3 used in Section 5.1.1 equation (35). We assume that the vertical shear can be
 4 expanded in even 4th-order Legendre polynomials:

$$5 \frac{\partial u}{\partial r} = p_0 + p_1 \frac{1}{2}(3\mu^2 - 1) + p_2 \frac{1}{8}(35\mu^4 - 30\mu^2 + 3), \quad (36)$$

6 where $\mu = \sin \theta$. Legendre polynomials may be preferred to the 4th-order poly-
 7 nomials used in Section 5.1.1 since the former are solutions to Laplace's equation on
 8 the sphere and are valid expansions at the poles. Now solve for the temperature
 9 profile:

$$\log \left(\frac{T(\theta, P)}{T_0(P)} \right) = - \frac{2\Omega r_0}{g} \int_{\theta_0}^{\theta} \sin \theta' \frac{du(\theta', P)}{dr} d\theta' \quad (37)$$

$$= - \frac{2\Omega r_0}{g} \int_{\theta_0}^{\theta} \sin \theta' \left(p_0 + p_1 \frac{1}{2}(3\mu^2 - 1) + p_2 \frac{1}{8}(35\mu^4 - 30\mu^2 + 3) \right) d\theta' \quad (38)$$

10 The integral on the right-hand side of can be solved analytically via repeated
 11 integration-by-parts. The final solution, written for brevity, is:

$$\log \left(\frac{T(\theta, P)}{T_0(P)} \right) = - \frac{2\Omega r_0}{g} (p_0 \cdot t_0 + p_1 \cdot t_1 + p_2 \cdot t_2) \quad (39)$$

$$T(\theta, P) = T_0(P) \cdot \exp \left[- \frac{2\Omega r_0}{g} (p_0 \cdot t_0 + p_1 \cdot t_1 + p_2 \cdot t_2) \right] \quad (40)$$

where:

$$t_0 = -\cos \theta$$

$$t_1 = \frac{1}{8} (\cos(3\theta) - 5 \cos \theta)$$

$$t_2 = \frac{1}{384} (-21 \cos(5\theta) + 55 \cos(3\theta) - 114 \cos \theta)$$

1 As before, this result be easily extended to the equator. In the following table,
 2 we compare the latitudes of the local maximal/minimal temperatures using this
 3 model and the model given in Section 5.1.1; we assume, for sake of example, an
 4 equatorial temperature of 80K.

Sect. 5.1.1 model	Appendix model
0 deg - 80.0K	0 deg - 80K
38.3 deg - 85.9K	33.5 deg - 84.4K
78.2 deg - 72.2K	70.5 deg - 76.0K

5 The qualitative analysis is the same between these models - the equator is colder
 6 than the mid-latitudes. The peak mid-latitude temperatures differ by 1.5K. While
 7 the model in Section 5.1.1 has a more extreme temperature change and is probably
 8 less accurate at high-latitudes, we do not consider this region in our analysis of
 9 Neptune's tropospheric temperature profiles since the zonal wind profile is wildly
 10 uncertain there - very few features are tracked in this region. Thus, the model
 11 presented in Section 5.1.1 is good enough as a base analysis - future work may
 12 explore better methods to model vertical wind shear on Neptune. We point out
 13 that analogous calculations can be used in the model presented in Section 5.1.2.

1 **10. Tables**

Poly. Profile	a (m/s)	b	c
Voyager	-398 ± 12	$1.88\text{E-}1 \pm 1.40\text{E-}2$	$-1.20\text{E-}5 \pm 3.00\text{E-}6$
H-band 2013	-325 ± 16	$1.58\text{E-}1 \pm 2.20\text{E-}2$	$-1.21\text{E-}5 \pm 4.67\text{E-}6$
K'-band 2013	-415 ± 42	$2.35\text{E-}1 \pm 5.34\text{E-}2$	$-2.23\text{E-}5 \pm 1.14\text{E-}5$
H-band 2014	-292 ± 29	$1.45\text{E-}1 \pm 4.91\text{E-}2$	$-1.18\text{E-}5 \pm 1.11\text{E-}5$
K'-band 2014	-433 ± 56	$2.40\text{E-}1 \pm 7.88\text{E-}2$	$-2.73\text{E-}5 \pm 1.90\text{E-}5$
Leg. Profile	a	b	c
H-band 2013	-159	462	37
K'-band 2013	-134	601	-127
H-band 2014	-95	359	76
K'-band 2014	-147	474	13

Table 1: Parameters in the fits to tracked zonal wind velocities. The fits are 4th-order polynomials given by: $V = a + b\theta^2 + c\theta^4$ (top half). For comparison, profiles generated from 4th-order Legendre polynomial fits given by: $V = a + b(3\mu^2 - 1)/2 + c(35\mu^4 - 30)/8$ where $\mu = \sin \theta$, are also shown (bottom half). The equatorial velocities derived from the Legendre polynomials are all well within the 2-sigma uncertainty given by the generic polynomial fits.

Variable	Description	Value
Ω	Rotation rate of Neptune (rad/s)	1.09E-4
g	Gravitational acceleration (m/s ²)	11.15
r_0	Neptune's equatorial radius (m)	2.4766E7
H	Scale height (km)	19.1 below 500 mbar 51.8 above 500 mbar
T	Temperature (K)	
u	Zonal velocity (m/s)	
θ	Latitude (rad)	
z	Radial distance into atmosphere (m)	

Table 2: List of variables and their values (if constant) used in the thermal wind equation.

Pressure (bar)	N	l^1 -norm	l^2 -norm
0.1	2	16.6724	14.4143
0.1	4	11.3805	8.1870
0.1	6	10.8843	7.0204
0.1	8	14.1867	10.2813
0.01	2	41.0348	81.8547
0.01	4	26.0158	39.5551
0.01	6	25.6478	37.7382
0.01	8	28.2277	39.3755

Table 3: Examples of the errors in the temperature fit to that derived from Voyager/IRIS spectra as a function of pressure and fit degree N. The l^1 -norm is the sum of the absolute difference between the observed and modeled data and the l^2 -norm is the sum of the squares of these differences.

1 11. Figures

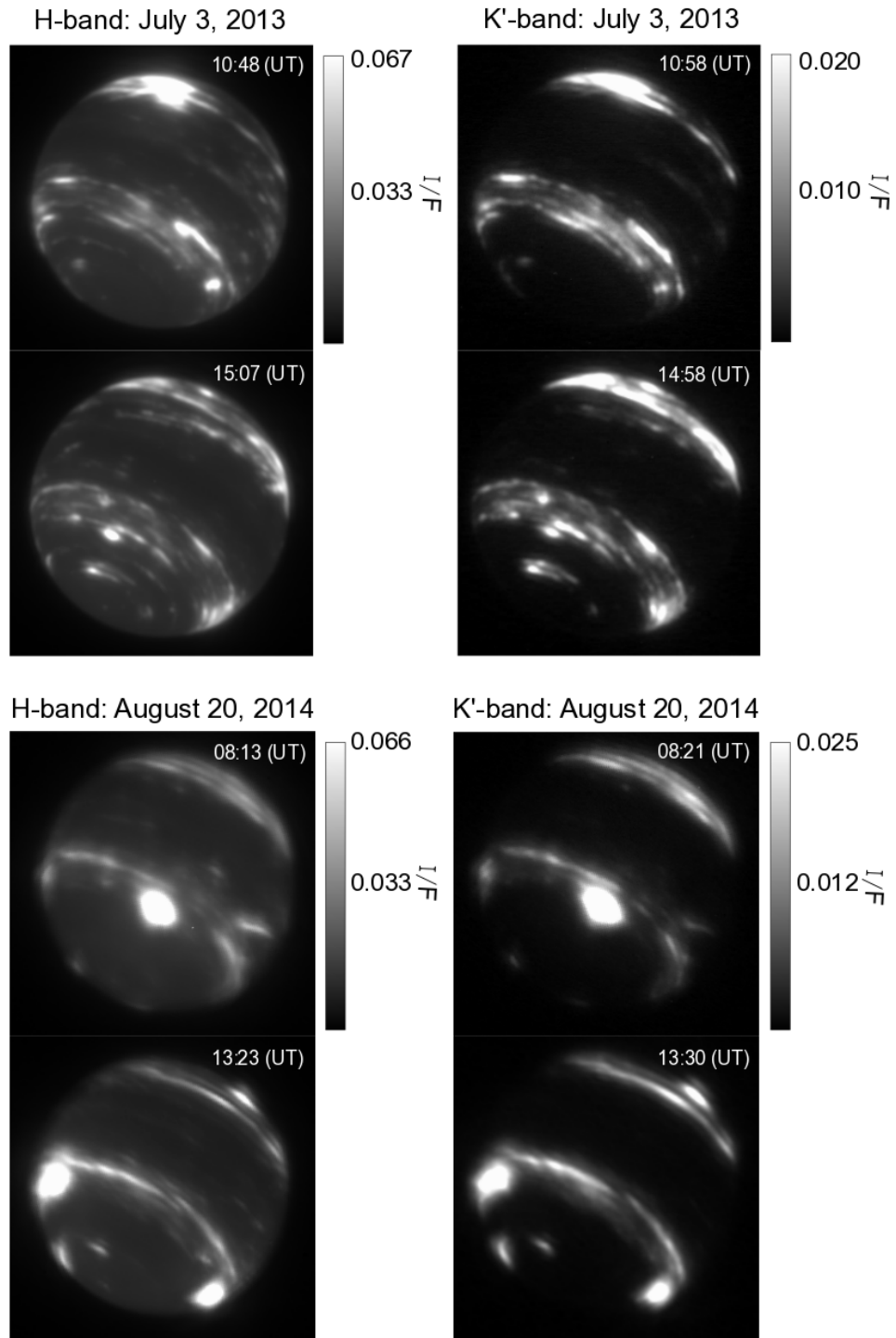


Figure 1: Images of Neptune taken in the H- (left columns) and K'- (right columns) taken on July 3, 2013 (top) and August 20, 2014 (bottom). The first and last images taken of Neptune on a given night are shown for each band. Images are in units of I/F with a colorbar given on the right of each image set.

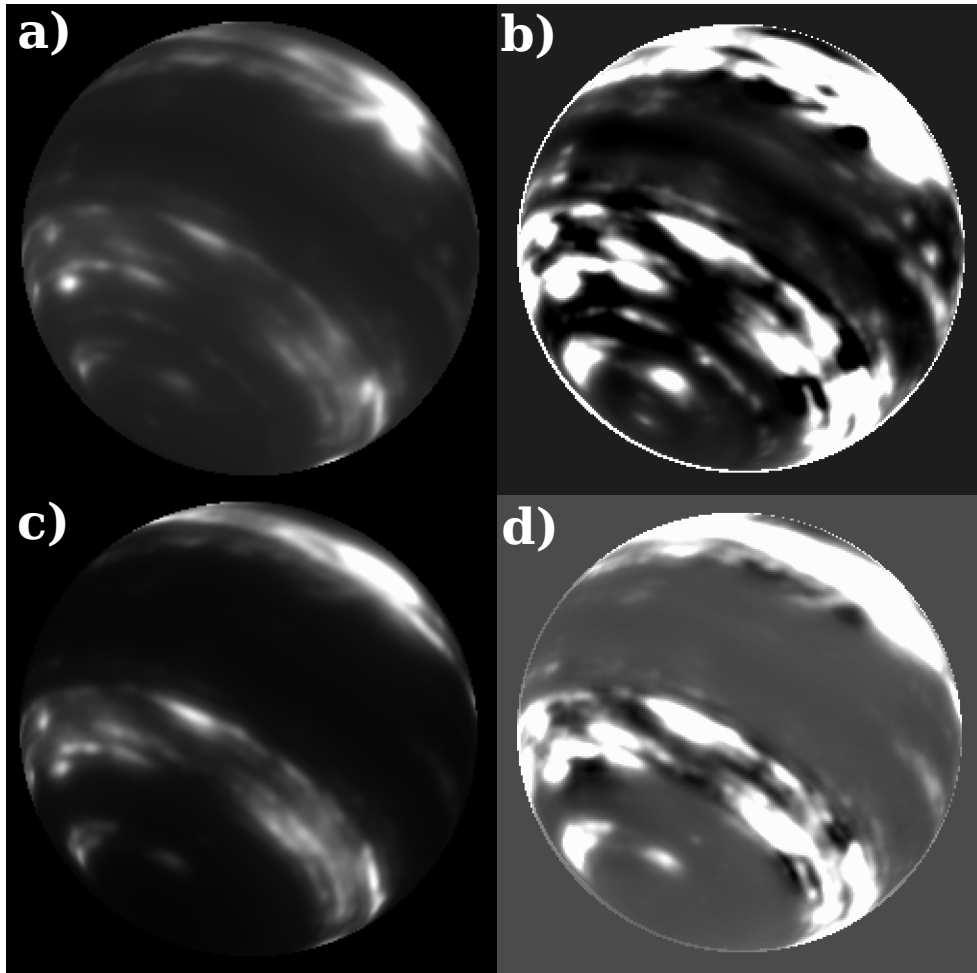
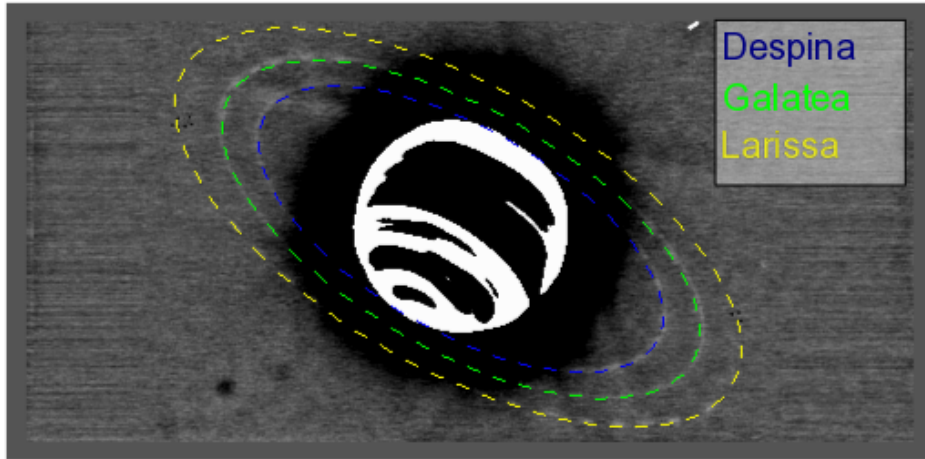


Figure 2: Images of Neptune in the H-band (top row) and K'-band (bottom row) on July 3, 2013 using the image combination method described in Fry et al. (2012). Figures a) and c) show the unaltered image while b) and d) show an enhanced, high-pass filtered version. Subtle equatorial features and banding can be made out due to the increased S/N ratio.

H-band: July 3, 2013 10:48-15:09 (UT)



K'-band: July 3, 2013 10:58-15:00 (UT)

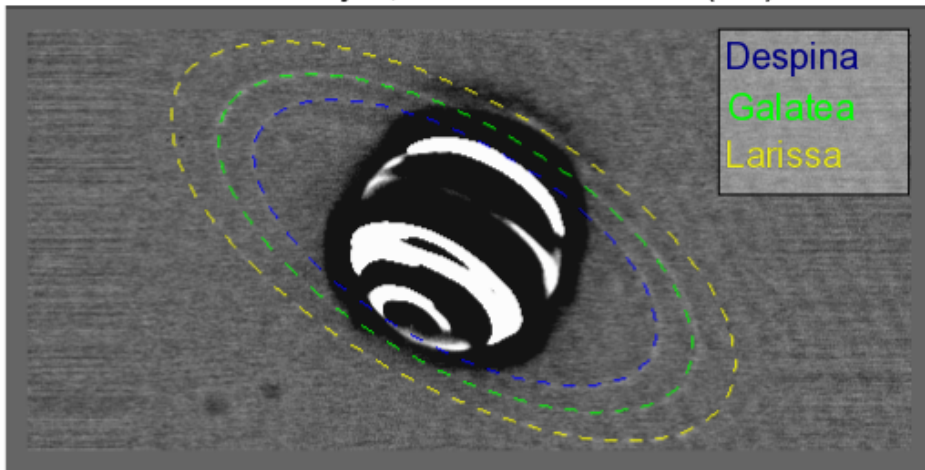


Figure 3: Mean averaged, high-pass filtered images of the aligned image stacks taken on July 3, 2013 in the H- (top) and K'- (bottom) bands. The colored dashed lines are the Ring Nodes orbits of three Neptunian moons (Despina, Galatea, and Larissa) and were used to determine the center of Neptune for navigation purposes. The path of each moon is seen as faint gray ellipses in these combined image stacks. The NASA orbits overlay the moon positions in the aligned images nicely, suggesting adequate navigation.

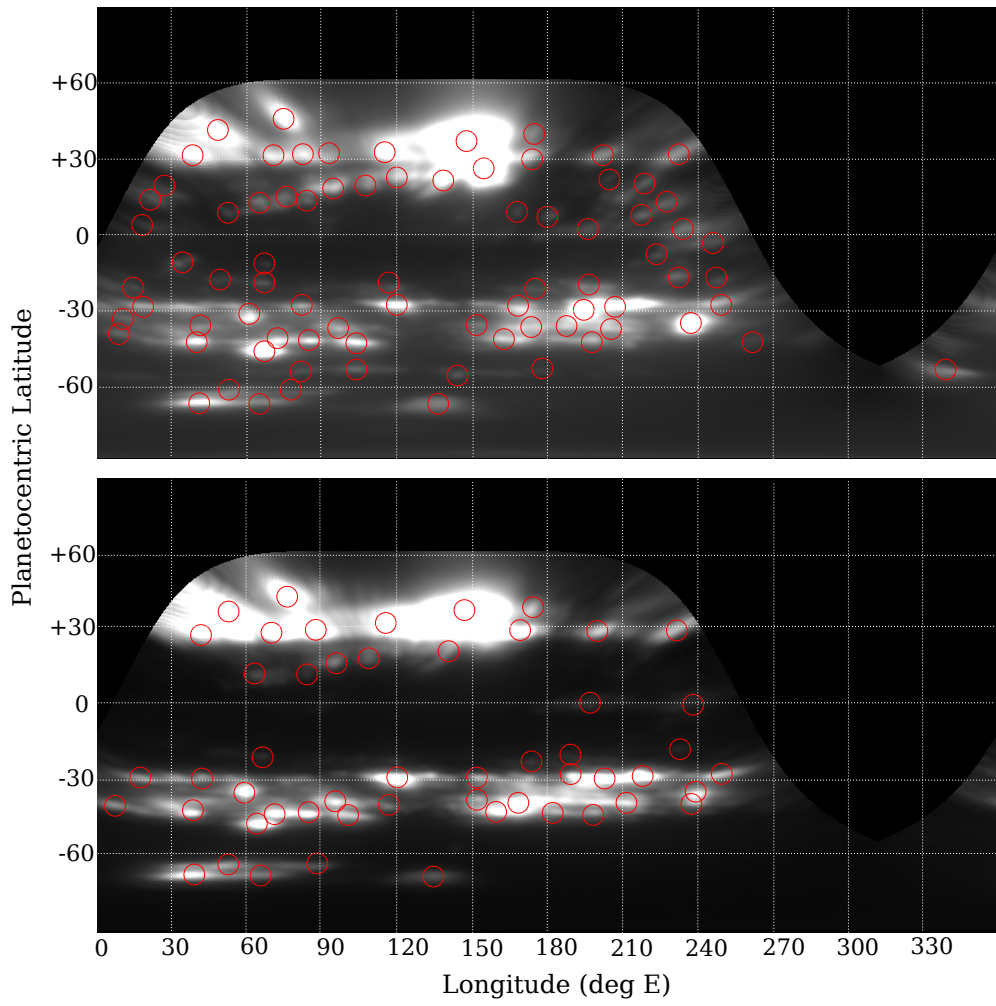


Figure 4: Rectangular projections of Figures 2a (H-band; top) and 2c (K'-band; bottom). Red circles are potential trackable features.

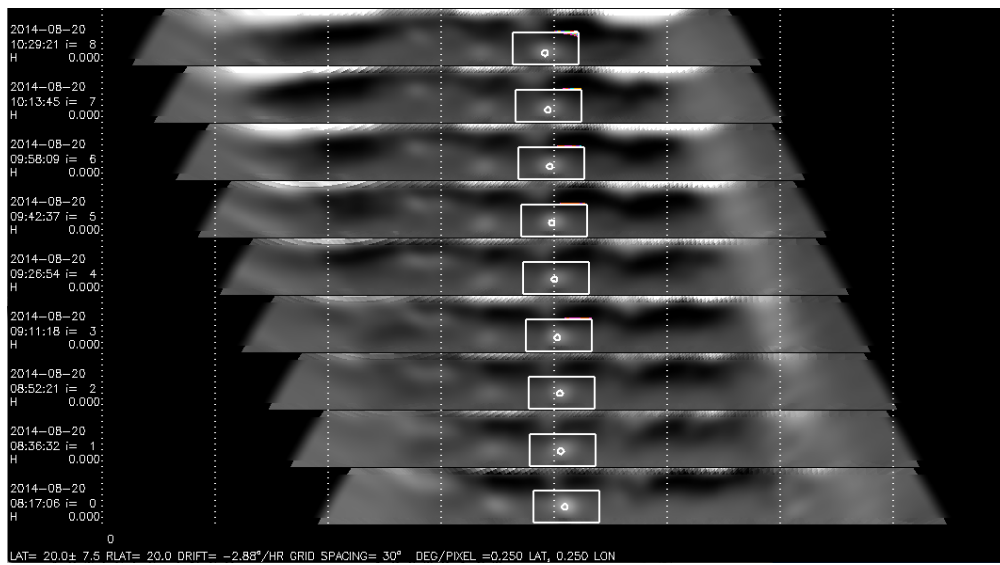


Figure 5: Example deprojected image strips at a fixed latitude range ($20^\circ \pm 7.5^\circ\text{N}$) stacked vertically by time since the initial observation. Each image strip is an average of a set of five images. Vertical white lines mark 30° increments in longitude. An example target feature of the tracking method is outlined in each box and its center is the result of maximizing the cross-correlation between image sets.

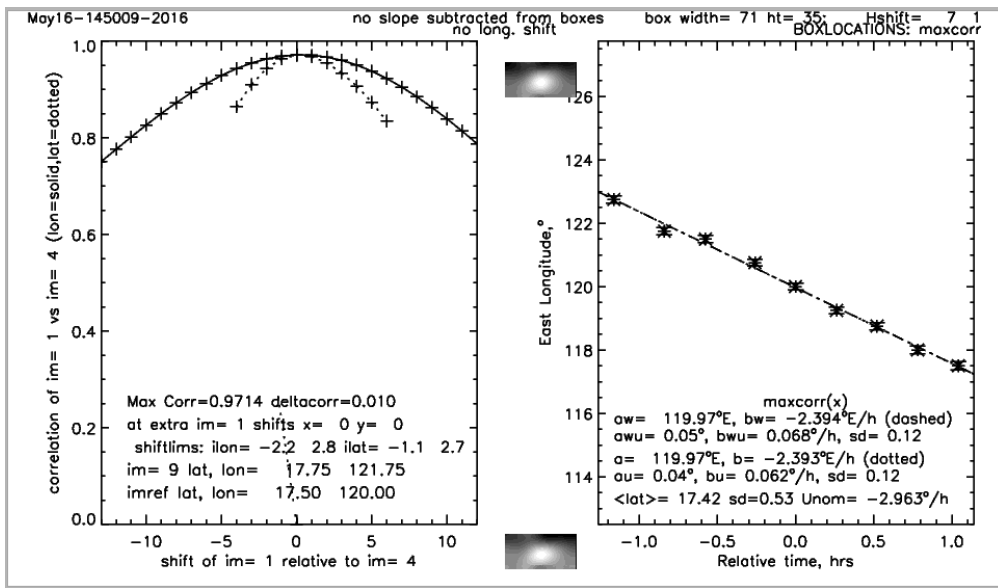


Figure 6: The output of the feature tracking method showing the predicted longitude positions (right) from maximizing the cross-correlation between image slices (left) for one particular feature (see Figure 5). Left: The solid lines are the correlation between longitudinal positions and the dashed lines are the correlation between latitudinal positions. Right: the black dots are the predicted longitude based on maximizing the correlation between image slices.. The dash-dot line is a line of best fit through the black (correlation) points. The selected feature at the initial and end frames is shown in the center.

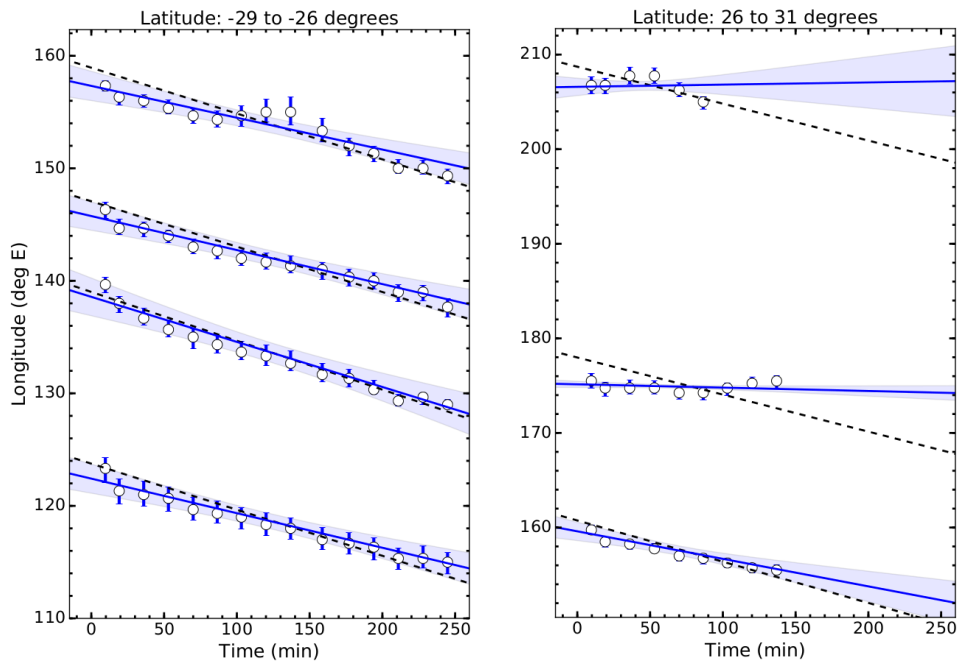


Figure 7: Selected feature tracking results in the H-band from July 3, 2013.. Each data point is a feature's derived longitude since the initial observation. The blue lines are lines of best fit to the data. The blue shaded region is the 1σ error in the fit. The dashed black line is the longitude path the feature would follow according to the canonical profile. The majority of tracked features follow the canonical profile (left figure), but some deviate significantly (right figure). Plots for all features can be found in Supplementary Materials 2.

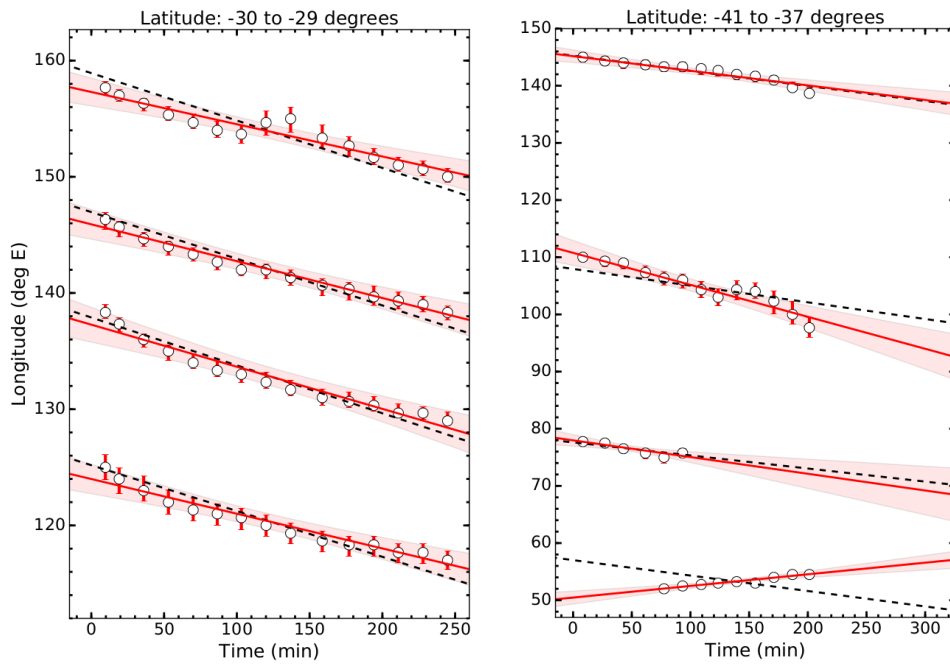


Figure 8: As figure 5 except for the K'-band. The red lines are lines of best fit to the data. The red shaded region is the 1σ error in the fit. The dashed black line is the longitude path the feature would follow according to the canonical profile. The majority of tracked features follow the canonical profile (left figure), but some deviate significantly (right figure).

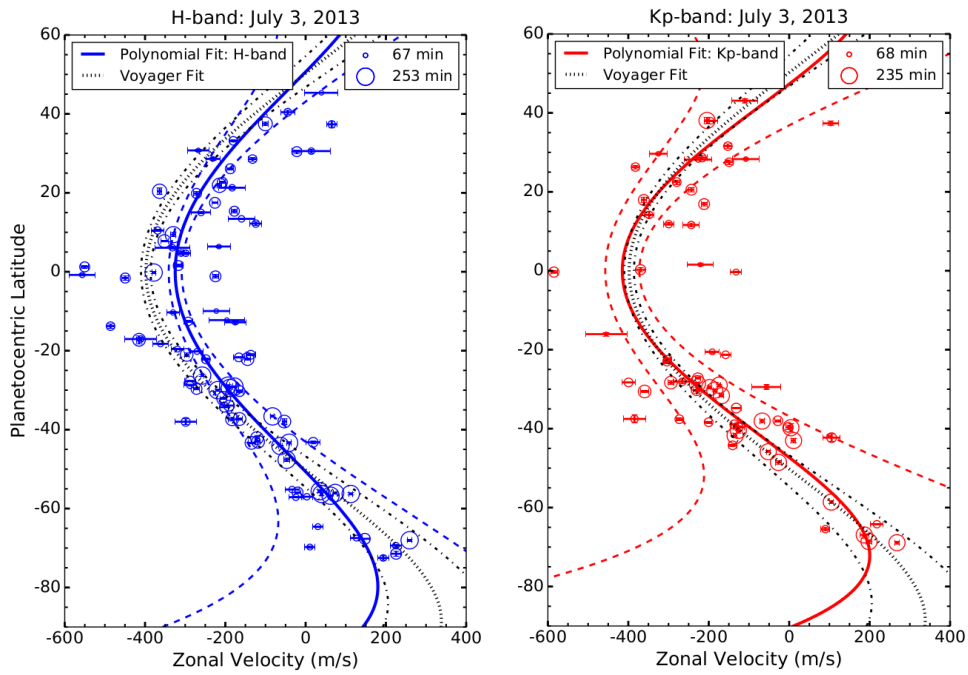


Figure 9: Eastward zonal wind velocities of tracked features in the H- and K'-band on July 3, 2013. Individual features are plotted as circles with their marker size proportional to the length of time the feature was tracked. The shortest and longest times are given in the top right corner. The Voyager profile is shown in a dotted black line with the width of uncertainty in a dot-dash black line. Our polynomial fit to the H-band is shown with a blue solid line (left image) while the fit to the K'-band is in red (right image). Their widths of uncertainty are in dashed blue and red lines respectively. There is significant positive deviation in the H-band wind speeds at the equator compared to those derived by the Voyager fit by 73 ± 16 m/s. The K'-band velocities agree well with the Voyager profile.

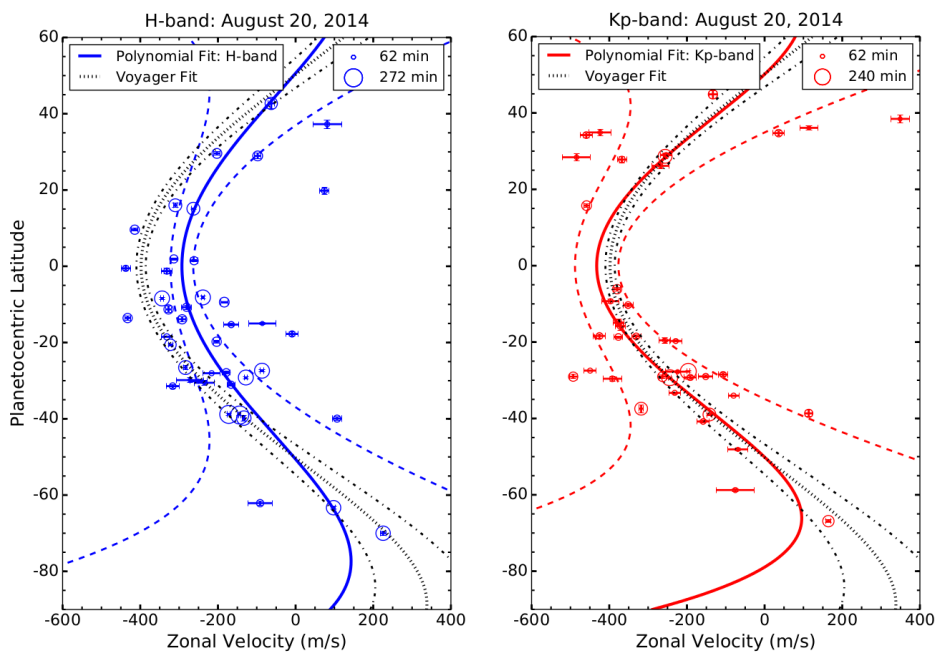


Figure 10: Same as figure 9 except for August 20, 2014. The Voyager profile is shown in a solid black line with the width of uncertainty in a dashed black line. Our polynomial fit to the H-band is shown with a blue solid line while the fit to the K^p-band is in red. Again, there is a significant positive shift in the H-band zonal velocities at the equator compared to those derived by Voyager by 93 ± 29 m/s.

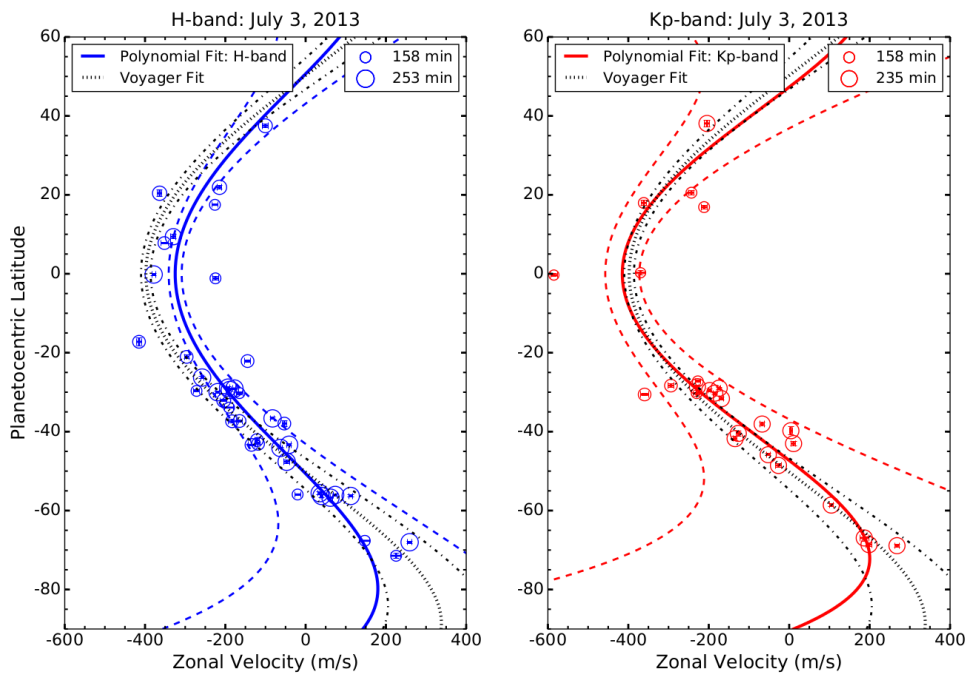


Figure 11: Same as figure 9 but only including features tracked in at least 10 images and with errors < 30 m/s.

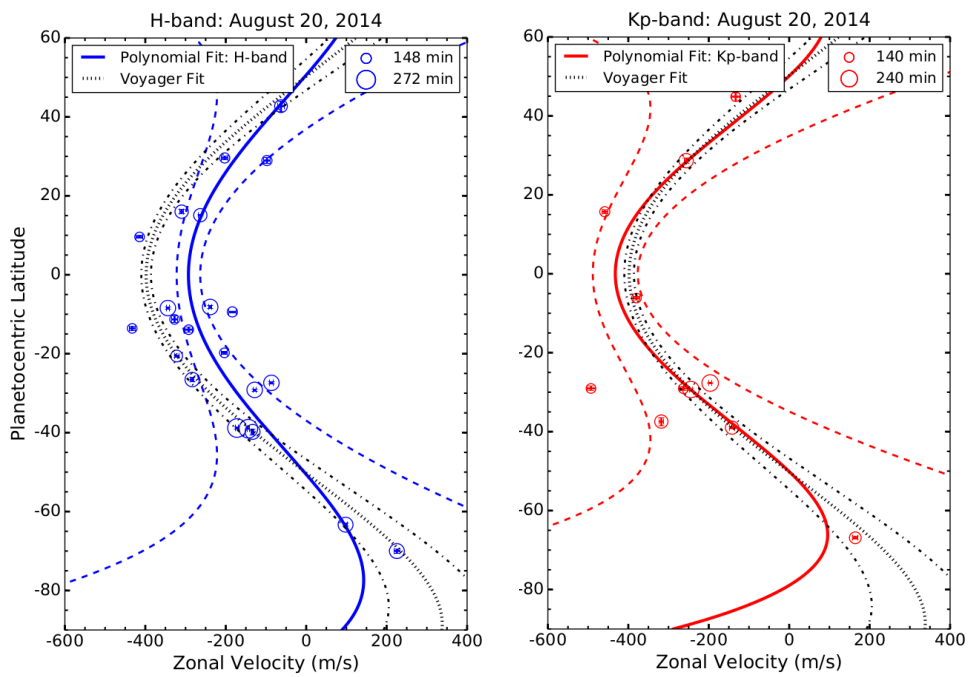


Figure 12: Same as figure 12 but only including features tracked in at least 10 images and with errors < 30 m/s.

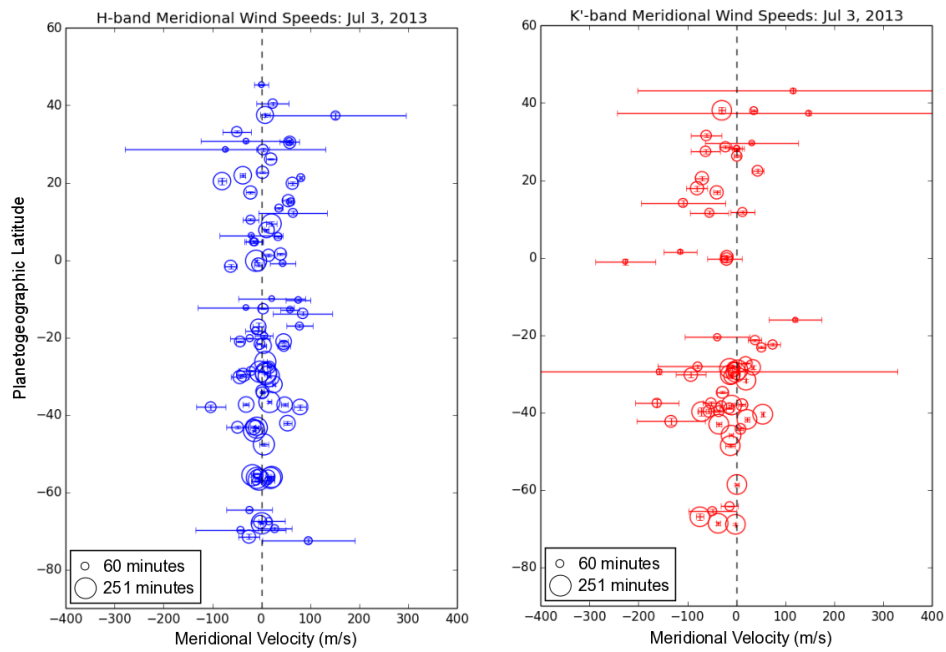


Figure 13: Meridional velocities of tracked features on July 3, 2013 with the H-band in blue on the left and the K'-band in red on the right. Circle size is proportional to tracked time with the shortest and longest times in the bottom left corners. The black dashed line marks zero and visually shows that the velocities are not too different from zero.

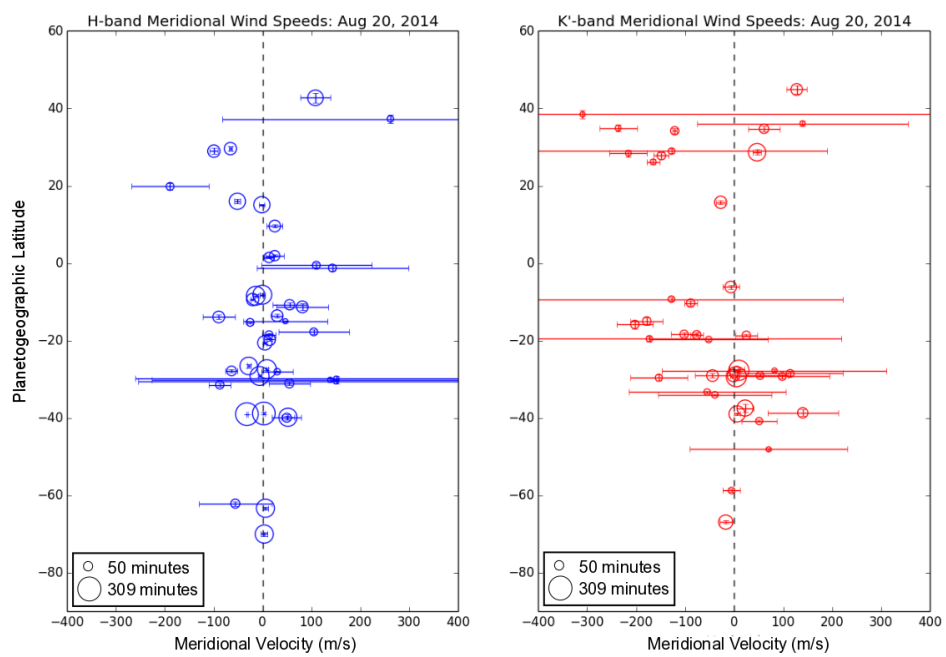


Figure 14: As figure 13 except for August 20, 2014.

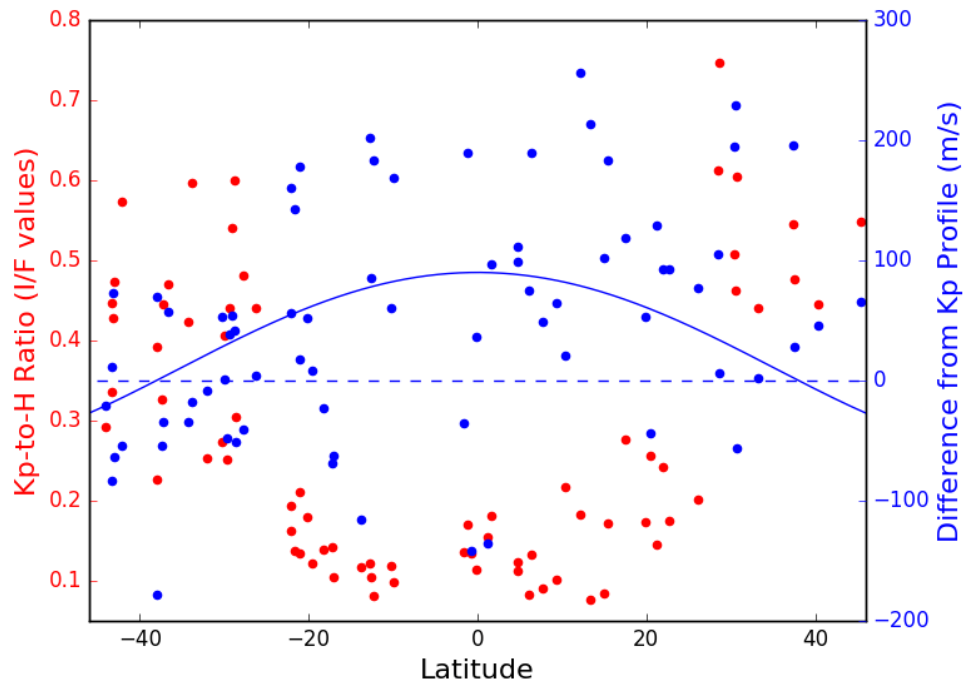


Figure 15: Derived K'-to-H I/F ratios vs. latitude (red) and zonal velocity deviation from the K' profile vs. latitude (blue) for 2013 H-band features. Shown are features between $\pm 45^\circ$. Positive values in velocity variation are eastward (less negative) relative to the K'-profile. Overplotted is the difference between the H and K' profiles (solid blue line) and the zero velocity difference (dashed blue line). Features in the equatorial region ($\pm 25^\circ$) have smaller K'/H intensities and larger velocity variations than those at mid-latitudes. This suggests that the shift in the H profile from the K' and canonical profiles is partly due to deep features.

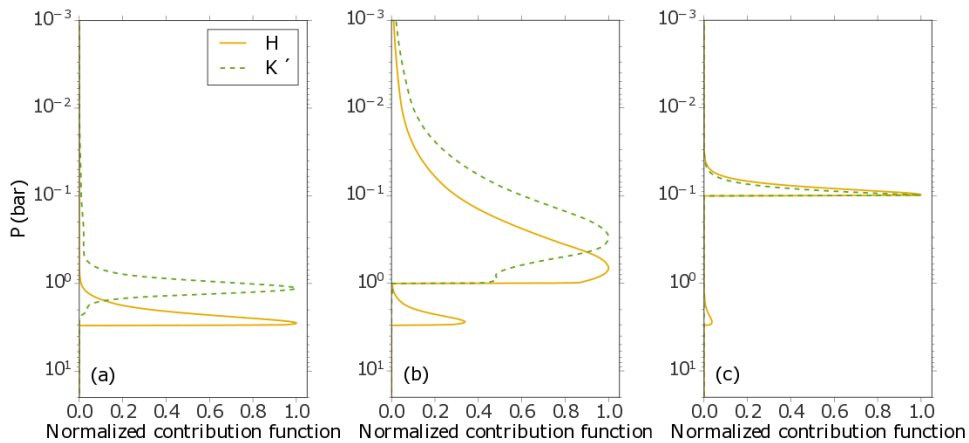


Figure 16: Normalized H-band (solid orange line) and K-band (green dashed line) contribution functions for three different model atmospheres, illustrating the range of depths from which the H- and K'- reflectivity may arise. In all three cases, gas opacity is contributed by collision-induced absorption of H_2 with H_2 , He, and CH_4 ; and by CH_4 absorption. Details of the atmosphere models may be found in Luszcz-Cook et al. (2015). The three models differ only in the assumed distribution of aerosols: all three models include a vertically thin cloud at 3 bar with a 1.6-micron optical depth of 0.5. In model (a), the atmosphere is clear aside from this 3-bar cloud. In model (b), there is an additional haze (scale height equal to that of the gas) between 1 bar and 1 mbar, with total 1.6-micron optical depth of 0.5. Model (c) includes the 3-bar cloud and an additional vertically thin cloud at 0.1 bar, also with a 1.6 micron optical depth of 0.5. Single scattering albedo and asymmetry factors are 0.75 and 0.7, respectively for all aerosol particles.

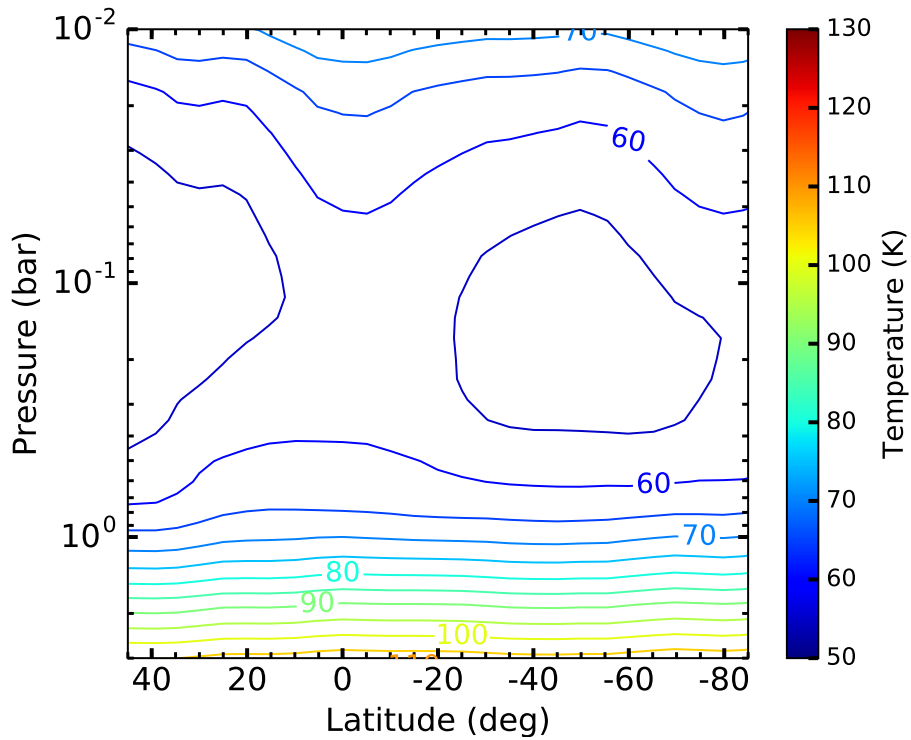


Figure 17: Temperature contours from inbound Voyager/IRIS spectra Conrath et al. (1991); Fletcher et al. (2014). This profile was used to determine the meridional temperature gradient.

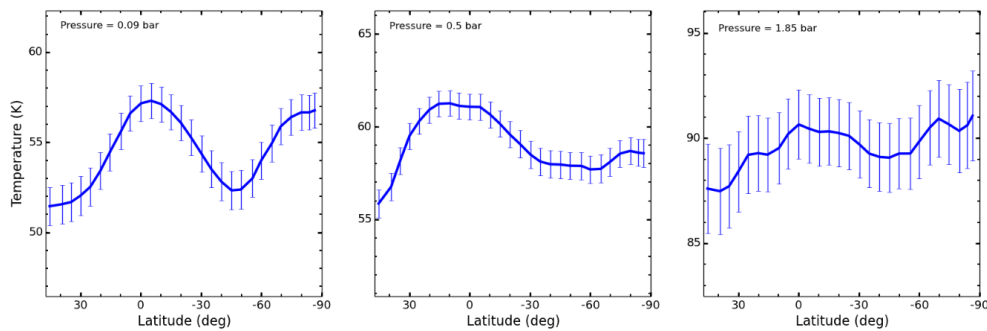


Figure 18: Meridional temperatures and errors at constant pressure from Fletcher et al. (2014). The first two images show Voyager/IRIS temperature retrievals that are within its sensitivity range (70 - 800 mbar). The latter figure is a temperature profile extrapolated from Voyager/IRIS results by the application of the smooth relaxation to an *a priori* profile. In this case, the uncertainty is substantial.

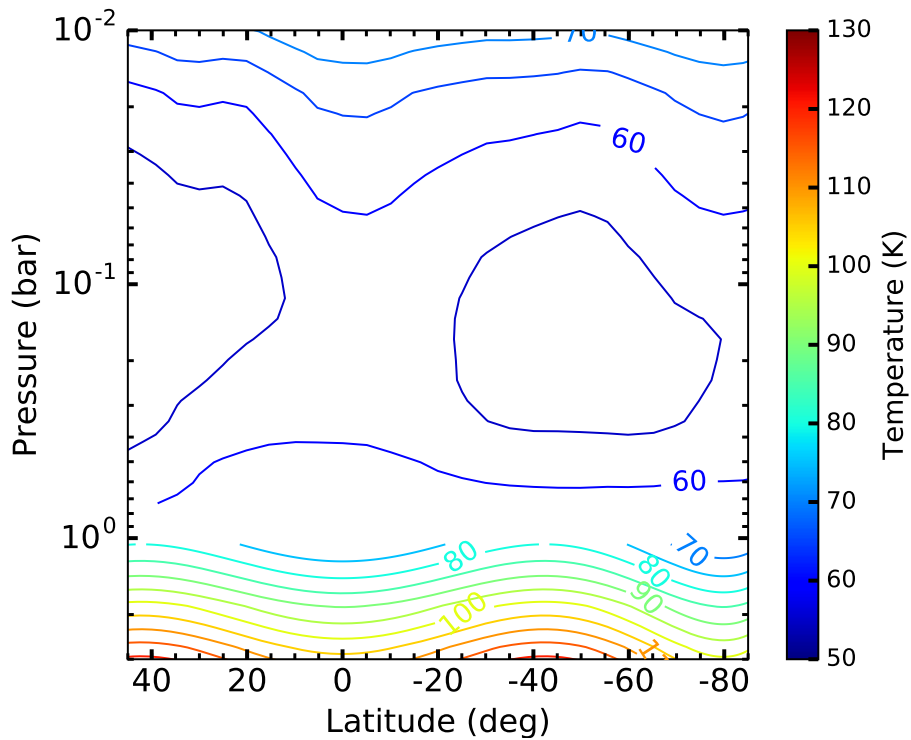


Figure 19: An example of the derived temperature profiles below 1 bar needed to produce the expected zonal wind differences between the H-and K'-bands. At a given pressure, the temperature at the equator was set to the mean global temperature. This is superimposed with the Voyager/IRIS temperature retrievals above 800 mbar. The region between 800 mbar to 1 bar region is left blank (without a temperature solution) to emphasize that a smooth transition between the the solution profile and the Voyager/IRIS profile is needed to avoid unphysical boundaries. For this example, the H-band profile was set at 1.3 bar and the K'-band profile at 10 mbar. In all tested solutions, the required difference between the equatorial and mid-latitude temperatures falls between 5-15 K.

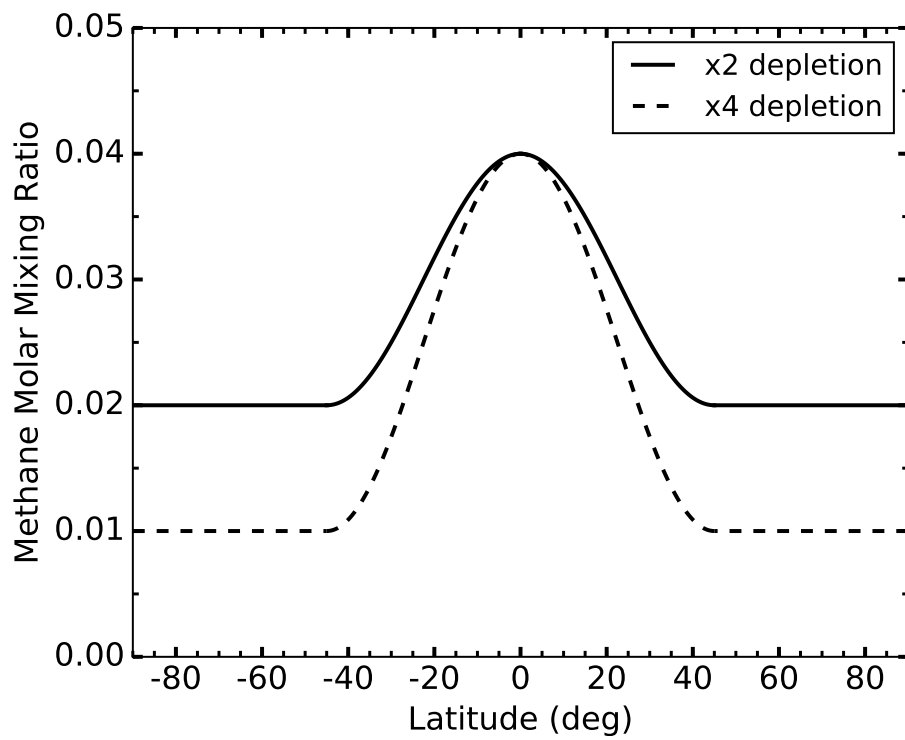


Figure 20: Plot of our methane model, given by equations (22) and (23).

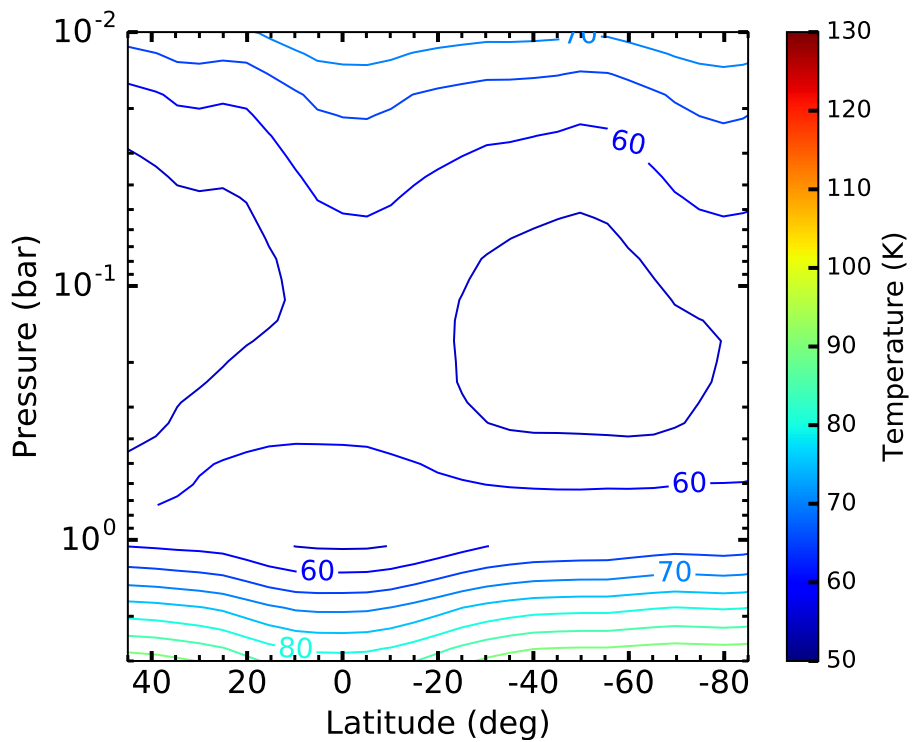


Figure 21: As Figure 17, except plotting the virtual temperature below 1 bar, assuming $\times 2$ depletion in methane at mid-latitudes and the poles. The virtual temperature is given by equation (28) and demonstrates the impact of methane gradients. A cold virtual temperature at the equator is produced, which is consistent with the expected sign of vertical wind shear.

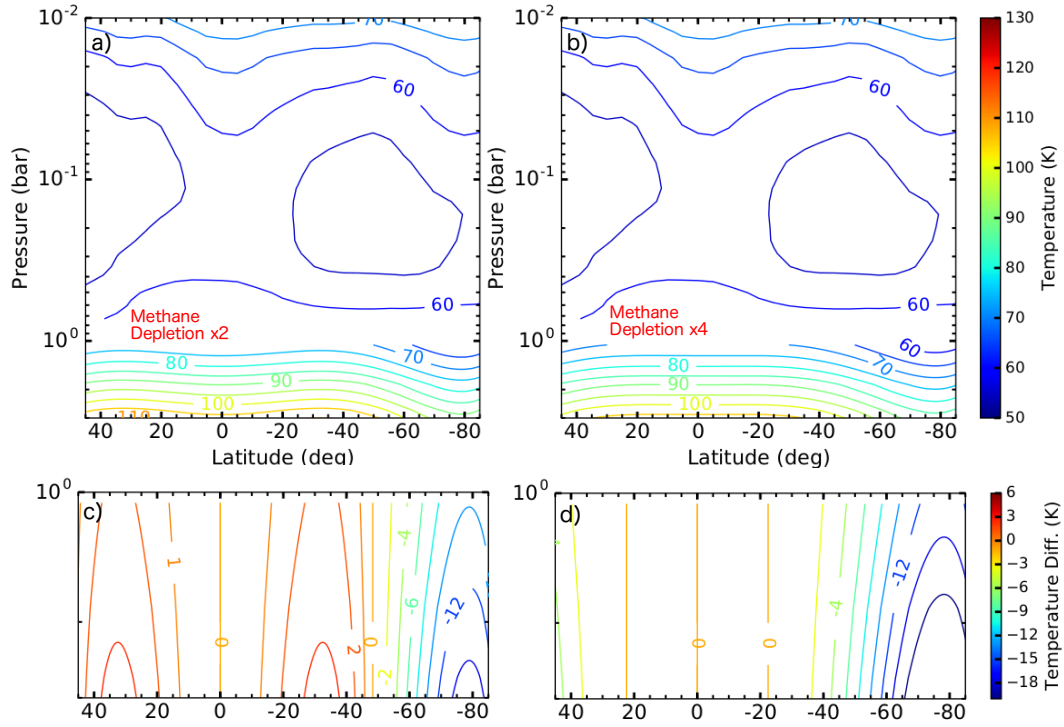


Figure 22: As Figure 19, but considering meridional methane variations in the thermal wind equation. a) Methane abundance depleted by 2× at mid-latitudes and poles (molar mixing ratio 0.02) compared to the equator (molar mixing ratio 0.04). b) Methane abundance depleted by 4× at mid-latitudes and poles (molar mixing ratio 0.01) compared to the equator and (molar mixing ratio 0.04). c) and d) show how the derived meridional temperatures deviate from the equatorial temperature along isobars, between 1–3 bar. c) corresponds to a) and d) to b). The low methane depletion (2×) case predicts an equator 2–3K cooler than the mid-latitudes. Higher depletion (4×) yields an equator 2–3K warmer than the mid-latitudes. These examples highlight how the meridional methane distribution affects the temperature gradient. In both cases, the H-band profile was set at 1.3 bar and the K'-band profile at 10 mbar.

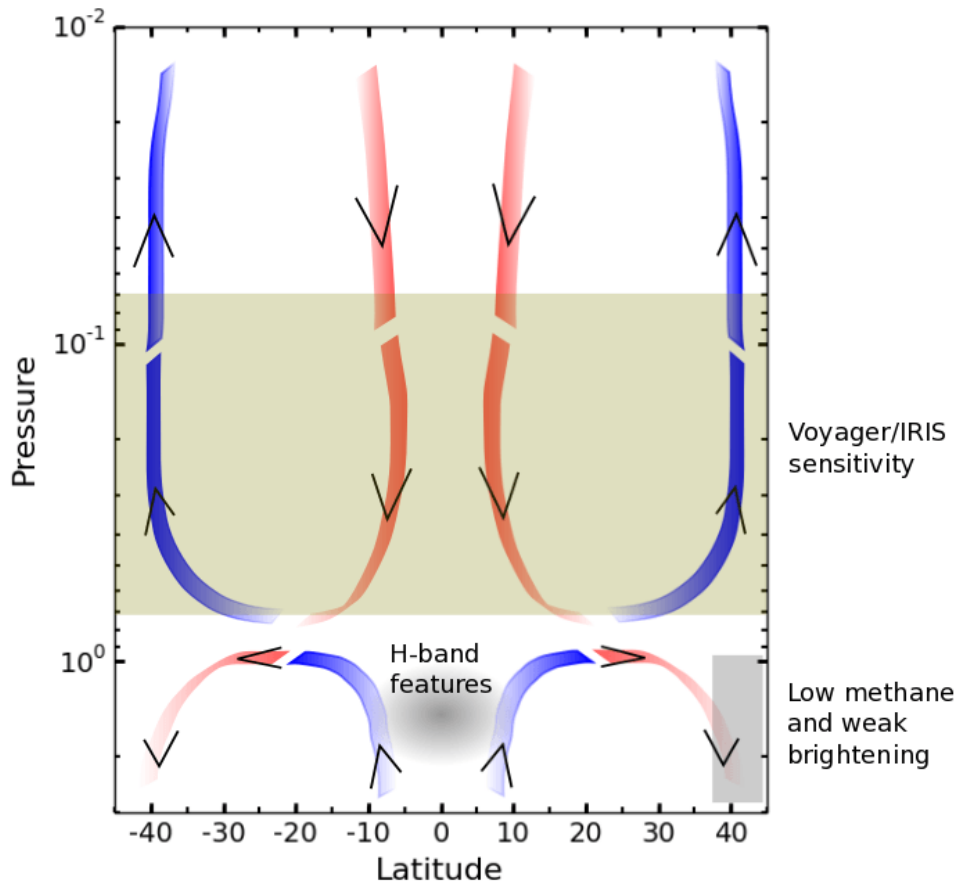


Figure 23: Schematic of our proposed circulation model between 10 mbar and 3 bar from the equator to mid-latitudes. The colored bands and arrows indicate the direction of circulation, blue indicating cool, rising air, and red warm, sinking air. Each cell forms a closed loop, continuing outside the range shown in the figure. The depth of circulation below 1 bar is unknown. The yellow band highlights the range of Voyager/IRIS sensitivity. The equatorial clouds seen in the H-band but not the K²-band are indicated as a gray circle. The mid-latitude region of methane depletion and weak brightening from Karkoschka and Tomasko (2011) and Butler et al. (2012) is represented by a gray rectangle.